university of groningen

Semi-Classical Energy Loss In EUV Plasma Generated Tin Ion Collisions With A Hydrogen Buffer Gas

Thomas Nieboer
Supervisor and 1st examiner: Prof. Dr. Ir. R. Hoekstra
2nd examiner: Dr. J. Sheil

August 27, 2024

Abstract

The stopping of tin ions originating from a laser produced plasma (LPP) in a hydrogen gas is of considerable interest for ASML's modern extreme ultra violet (EUV) lithography machines. Near the LPP, EUV collector mirrors are placed which have shown to deteriorate from exposure to energetic tin ions Sn^{q+}. A promising solution is to add a hydrogen buffer gas in LPP chamber. However the interaction and stopping power of Sn^{q+} with H_2 is still not fully understood. This makes it difficult to determine the minimum necessary H_2 pressure for total stopping. In this research a semi-classical collision model called Groningen Ion Stopping (GIonS) has been improved with the adoption of DFT interaction potentials for Sn^{1+}, Sn^{2+}. Stopping results have shown close resemblance with what has been found by Abramenko et al. in 2018. Additionally some heavily debated characteristic features in the Abramenko data, such as a dip in Sn^{2+} stopping cross-sections from initial energies of 4 keV upwards, can be further brought into question. This project shows that the description of stopping through a collision model with DFT based potentials is a valid and promising method to further study tin ion - hydrogen interactions.

Contents

1 Introduction

Every year the demand of computing power increases drastically , with the introduction of large datacenters power consumption of the computer chips used is starting become a relevant factor as well [1, 2]. This poses a substantial challenge for the semi-conductor industry as not only are chips required to become more powerful and energy efficient but also more compact. At the frontier of developing such chips are ASML's extreme ultraviolet light (EUV) nanolithography machines which are able to make the most advanced computer chips in the entire world. ASML EUV machines are extremely complex and one of the more impressive processes taking place within the machine is the production of 13.5 nm light through plasma formation.

In ASML's machines liquid tin microdroplets are released periodically into a vacuum chamber. In this vacuum vessel 13.5 nm light is produced through the creation of a so called Laser Produced Plasma (LPP). An LPP is formed through a combination of two CO_2 10 μm light laser pulses that hit the released tin droplet in quick succession [3, 4]. Tin ions, Sn^{q+}, of many different charge and excited states rapidly fly outward from the LPP during which a broad band of light is emitted through de-excitation [5]. The desired 13.5 nm light is subsequently focused through a set of collector mirrors [4, 6, 7] lining the inside of the vacuum chamber. After the light has passed another few focusing mirrors it will be used as the light source for photolithography processes further on in the machine.

The LPP produces the necessary EUV radiation but also generates plasma debris consisting of droplet fragments and fast ions [3, 4, 8]. From this plasma debris, the tin ions are thought to be the most threatening to the lifetime of the collector mirrors [4, 8]. To mitigate this solutions aimed at deflecting tin ions with magnetic fields [9, 10, 11] or stopping them with a background gas are being developed. A good choice of background gas has been found to be H_2 as it is fairly transparent to 13.5 nm EUV light [12], however determining the pressures needed to sufficiently stop the tin ions is still important to minimize intensity losses of the EUV light. In order to obtain a well funded minimal needed operating pressure in-depth knowledge of the stopping capabilities of tin and hydrogen is needed.

Stopping is a medium's ability to slow down incoming projectiles. This can be characterized as the amount of energy a projectile with some set kinetic energy loses when traversing a unit distance through the medium and is called the stopping power. Because stopping power is dependent on the mediums density, it is often more convenient to talk about stopping cross-sections [13], which is the stopping power normalized to the target mediums particle density. The difference between stopping cross-sections and power is merely a constant, as such when stopping is mentioned from now it could refer to either of the two.

Theoretically stopping can be divided into several stopping regimes, nuclear stopping at the lower energy regime which is described by the hard sphere and Thomas-Fermi-Molière theories, and at higher energies electronic stopping as expressed by Linhard-Firsov and Bethe-Bloch theory [13], see figure 1. Especially when dealing with lower initial energies, quantum effects such as electron transfer could play an important role in the energy transfer mechanism which would require a more case specific approach.

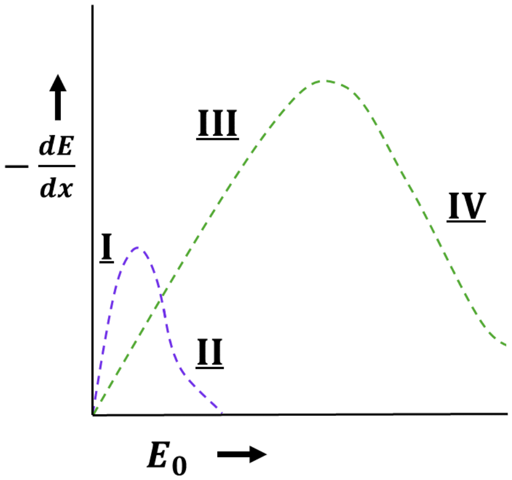

Figure 1: *Schematic depiction of different stopping regimes with on the y-axis, **I**: Hard sphere, **II**: Thomas-Fermi-Molière, **III**: Linhard-Firsov, and **IV**: Bethe-Bloch.*

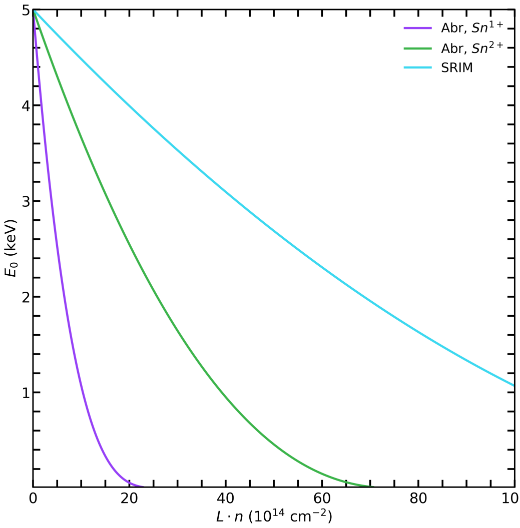

Figure 2: *Stopping length times gas density of 5 keV tin ions with a hydrogen gas as indicated by Abramenko's experimental stopping cross-section data and SRIM's predicted stopping cross-sections.*

As of writing this thesis only one experiment carried out by Abramenko et al. in 2018 [8] has determined stopping cross-sections of Sn^{1+} and Sn^{2+} with H_2. Comparing SRIM stopping data and comparing it against the functional fits obtained from the Abramenko data shows a big disagreement in predicted stopping length of a tin ion in hydrogen gas, figure 2. Furthermore the SRIM simulations use the general screened Ziegler-Biersack-Littmark (ZBL) potential [14] (see eq (1)) which does not differentiate stopping of the tin ions based off of their charge state which is seen to be different in Abramenko's results. The reason for the difference in stopping behaviour between charge states has been thought to originate from electronic configuration. Making a tailored molecular dynamics (MD) code that uses a custom made quantum potential to calculate stopping lengths could resolve the discrepancy between theory and result.

$$\begin{aligned} V_{\mathrm{ZBL}}(r) =& \frac{Z_t Z_p}{r}\left(0.1818e^{-3.2\frac{r}{a_u}} + 0.5099e^{-0.9423\frac{r}{a_u}} + 0.2802^{-0.4028\frac{r}{a_u}} + 0.02817e^{-0.2016\frac{r}{a_u}}\right) \\ \text{with, } a_u =& \frac{a_0}{Z_t^{0.23} + Z_p^{0.23}} \end{aligned} \tag{1}$$

In this thesis the goal was set to calculate a density functional theory (DFT) based interaction potential and implement it within the pre-existing Groningen Ion Stopping Version 1 (GIonS V1) code. GIonS is an in house build MD code originally made to study the effect of electron transfer on energy losses in groundstate $Sn^{q+} - H_2$ collisions. In it's first iteration it used the ZBL and Coulomb potentials depending on the charge state of the H_2. Ground-states of $1+, 2+$ tin ions do not have electron transfer during collisions resulting in V1 only using the ZBL potential resulting in stopping lengths, similar to SRIM. Even more importantly V1 does not discern stopping between the $1+, 2+$ charge states. For the second iterations of the code, GIonS V2, it was decided to continue with ground-state calculations but introduce DFT interaction potentials, these were constructed using the NWChem DFT-code [15]. The data points retrieved for interaction potential function construction were subsequently interpolated with two conveniently defined sparse grids which were implemented using the Tasmanian sparse grid package [16, 17]. Additionally the choice was made to improve the description of H_2 as a point particle in V1, to a fully fledged molecule with an orientation in V2. The exact method with which the H_2 is treated in the improved model will be elaborated upon in the theory section. The most important improvement this introduces is the ability to use non-center symmetric potentials in the MD simulations. Furthermore the orientation of the hydrogen molecule was also used to study the possible effect of rotational motion on the collision paths.

With the fundamental improvements posed by GIonS V2, classical Sn^{1+}, Sn^{2+} - H_2 collision paths were calculated for initial energies in the range $0.01 - 10$ keV. These were in turn used to find the stopping cross-sections of Sn^{1+}, Sn^{2+} and compared with experimental results.

2 Theory

At the basis of understanding the workings of $\mathrm{Sn}^{q+} - \mathrm{H}_2^+$ collisions from a classical perspective is the correct description of dynamics [13]. In the master thesis introducing GIonS V1 the dynamic picture was build up from billiard ball type collisions to long range interactions to a description based on the interaction potential of the system. In this thesis we pick up where GIonS V1 ended while introducing some concepts worth repeating along the way. Subsequently a connection between average energy loss per collision and stopping cross-section will be made as well.

2.1 Dynamics

2.1.1 Momentum Transfer

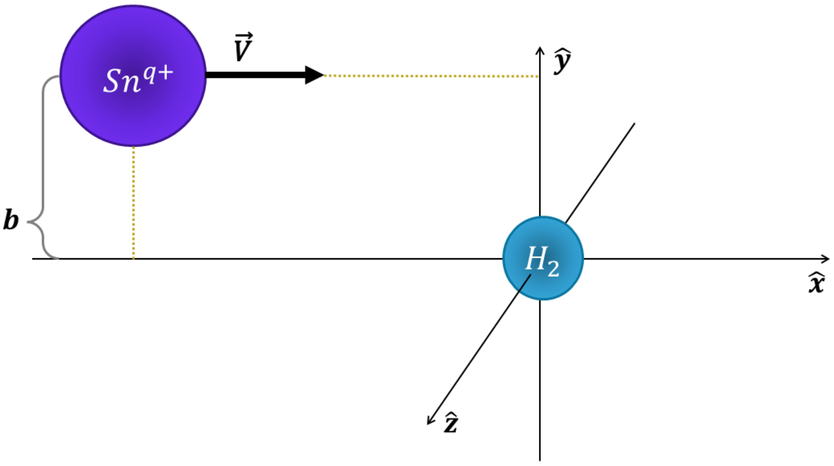

Figure 3: *Illustration of the initial conditions that uniquely describe a collision, with impact parameter b and velocity/energy $\mathbf{V} \rightarrow E$.*

The goal of the GIonS project is to correctly model stopping between a heavy projectile of mass m_p and light target of mass m_t. In GIonS this is achieved by modeling classical trajectories based off of the interaction one would expect between projectile and mass. If we have a Sn^{q+} ion with maximally 10 KeV of kinetic energy it would have a speed $|\mathbf{v}| \sim 5 \cdot 10^{-3}c$, showing that we are operating withing the classical regime. From basic level billiard type interaction it can be shown that the energy transfer during a collision $\Delta E \propto \frac{m_t}{m_p}$ if $m_p \gg m_t$, indicating that heavier targets might be better at stopping ions. In reality the interaction between nuclei is determined by their respective interaction potential V, such as the Coulomb or the aforementioned screened type potentials. The relation between ΔE and the involved masses might be very different with more realistic interactions, especially when they take into account electronic configuration of both projectile and target.

Using the elementary formula, eq (2), the force vectors can be found from the potential used.

Repeating this for each time step and moving the particles accordingly will give the expected collision path and energy transfer.

$$\mathbf{F} = -\nabla V(\mathbf{r}) \tag{2}$$

In the first iteration of GIonS the charge transfer effect was modeled in, effectively changing the potential if an electron got absorbed by the tin ion. For the second iteration the main effort was put into finding as accurate as possible potentials as their functional form heavily influences the energy loss function. As will be shown shortly any error in the energy loss function manifests itself in the predicted stopping power of projectile-target combination as another error. Thus an accurate interaction force is crucial for predicting stopping powers and lengths.

2.1.2 Molecular Hydrogen

By going from a point particle description to a 3D-homonuclear diatomic molecule, the center symmetric nature of the interaction potential is lost. Suddenly orientation of the H_2 with respect to the incoming Sn^{q+} starts to matter in the energy loss per collision. To this effect a specific set of coordinates was used to describe the initial state of the system. The definition of the coordinates is depicted in figure 4. Notably the introduction of H_2 orientations requires the introduction of an out of plane angle forcing the use of 3D vectors in simulating these type of collisions.

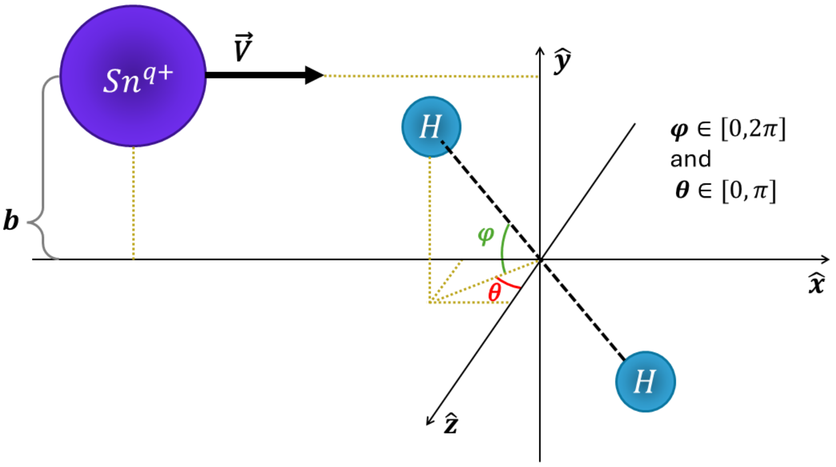

Figure 4: *Illustration of the initial conditions that describe a collision with a 3D* H_2*, with impact parameter* b*, velocity/energy* $\vec{\mathbf{V}} \to E$*, and in* xy*-plane angle* ϕ *and out of plane* θ*.*

Naturally this also implies that for any type of observable that is calculated from GIonS V2 the average should be taken over all possible orientations. If angular n, m steps of $\Delta\phi$ and $\Delta\theta$ are taken, this implies calculations of:

$$\begin{gathered}\Phi_n = \{x \in \mathbb{R} \mid 0 < x < \pi - \Delta\phi \wedge \tfrac{x}{\pi} \in \mathbb{N}_0 \wedge \tfrac{x}{\Delta\phi} < n\} \\ \Theta_m = \{x \in \mathbb{R} \mid 0 < x < \tfrac{\pi}{2} \wedge \tfrac{x}{\pi} \in \mathbb{N}_0 \wedge \tfrac{x}{\Delta\theta} < m\}\end{gathered} \tag{3}$$

as the symmetry in the x, y-plane reduces the points needed in Θ_m. Additionally for $\theta = 0$ the result will be the same regardless of ϕ meaning some more calculation can be skipped. With these set of points the weights of the corresponding orientations are not taken into account. If N-orientations are to be simulated a weight can be defined:

$$w(\phi, \theta) = \begin{cases} 1/W_{nm} & \text{if } \theta = 0, \frac{\pi}{2} \\ 2/W_{nm} & \text{otherwise,} \end{cases} \tag{4}$$

where W_{nm} is chosen such that:

$$\sum_{\phi \in \Phi_n} \sum_{\theta \in \Theta_m} w(\phi, \theta) = 1 \tag{5}$$

Furthermore the linear nature of the H_2-molecule forces an accurate description of the inter nuclear separation d between two hydrogen atoms. In GIonS V2 this was taken to be the bondlenght of ground-state H_2, being $d \approx 1.4$ atomic units (a.u.) and H_2^+ having $d \approx 2.0$ a.u. [18]. During a collision d might change over time due to several processes, the first being electron transfer. If an electron is captured by a tin ion, what happens with d while $H_2 \rightarrow H_2^+$ is quite unclear. The relaxation of the bond from 1.4 to 2.0 might take place within a time frame way larger than the characteristic time of a collision with some initial Sn^{q+} energy E_0. In such circumstances the assumption that the bondlength stays constant seems reasonable. On the other hand if E_0 is small enough this assumption won't hold.

Secondly, during the collision a change in electron configuration might also allow for the relaxation of the hydrogen bond. Whether this is significant for the trajectories of the particles is in itself an open question. And once again it is not yet clear how much time is needed for this process to occur. For the sake of keeping this project somewhat simple the decision was made to use the simplified situation that a constant bond length offers even if this is only a first approximation. In the discussion some reflection will be included that anticipates the possible effects a changing bond length might induce.

With a completely rigid bond, rotational motion is added as additional dynamics. Just like velocity, the angular velocity of H_2 can be updated every time step in a simulation. For that the torque at any time-step needs to be determined. In classical motion torque around an axis labeled with i is calculated using:

$$\boldsymbol{\tau}_i = \int_V d^3 r' \mathbf{r_i}' \times \mathbf{F}(\mathbf{r_i}') \tag{6}$$

where $\mathbf{r'}_i$ denotes the vector from the rotational axis i to the point where a force is applied. For the hydrogen molecule this formula is substantially simpler as only two forces need to be considered, the force on hydrogen atom 1 and hydrogen atom 2. Logically the axis of rotation runs through the center of mass and perpendicular to the bond axis of H_2. The center of mass is not anchored making it more difficult to imagine how the total motion of the molecule works out. The proposal is to calculate the two H-forces, find the components perpendicular to the bond length $\mathbf{F_1}, \mathbf{F_2}$ and from that find what is called the coupled torque $\boldsymbol{\tau}_c$. The coupled torque is the torque created when on the two opposite sites of the hydrogen atom, there are two forces that are anti parallel and (partially) cancel out as depicted in figure 5. Crucially the rigid bond allows us to attribute any remaining components from the perpendicular and parallel force vectors to the movement of the center of mass.

$$\boldsymbol{\tau}_c = \begin{cases} 2\left(\frac{\mathbf{d}}{2} \times min(|\mathbf{F_1}|, |\mathbf{F_2}|)\right) & \text{if } \mathbf{F_1} \text{ and } \mathbf{F_2} \text{ are anti parallel} \\ 0 & \text{otherwise,} \end{cases} \tag{7}$$

In GIonS V2 the decision has been made to calculate the total motion of H_2's center from the normal ZBL/Coulomb/DFT potential and the rotational motion independently. To combine the two motions only the angular velocity of the latter is extracted and added to the center of mass motion. This will undoubtedly break conservation of energy, which needs to be addressed. Lets say that during a time-step dt, a force $\mathbf{F}$ is applied and a rotational energy difference of ΔE_{rot} is created due to torque. To make sure energy is conserved we need to rescale the interaction force to $\mathbf{F}'$. $\mathbf{F}'$ is constrained by the following condition,

$$\tfrac{1}{2}\left|\mathbf{v}_0 + \frac{\mathbf{F}_i}{m}dt\right|^2 = \tfrac{1}{2}\left|\mathbf{v}_0 + \frac{\mathbf{F}'_i}{m}dt\right|^2 + \Delta E_{rot}\frac{m_i}{m_{\mathrm{Sn}} + m_{\mathrm{H}_2}} \tag{8}$$

Where here the index i refers to the frame of either Sn^{q+} or H_2. Because the direction of $\mathbf{F}'_i$ is unknown some assumptions must be made to solve for $\mathbf{F}'_i$. By making the reasonable assumption that F_i and F'_i are in the same direction, we write, $\mathbf{F}'_i = a_i\mathbf{F}_i$ and by filling this into (8) a quadratic equation in a_i is formed. Solving for a_i for both $i = \mathrm{Sn}^{q+}, \mathrm{H}_2$ we get the corrected force $\mathbf{F}'_i$ for a time-step, that is still energy conserving. By solving the trajectories in this manner GIonS could tell us something about the relevance of the rotational motion to stopping power. For electron transfer it will likely be important as the energy crossing contour used for Landau-Zener calculations is no longer center symmetric in the DFT potential, by spinning of the H_2 the crossing could be crossed earlier or later on in the collision.

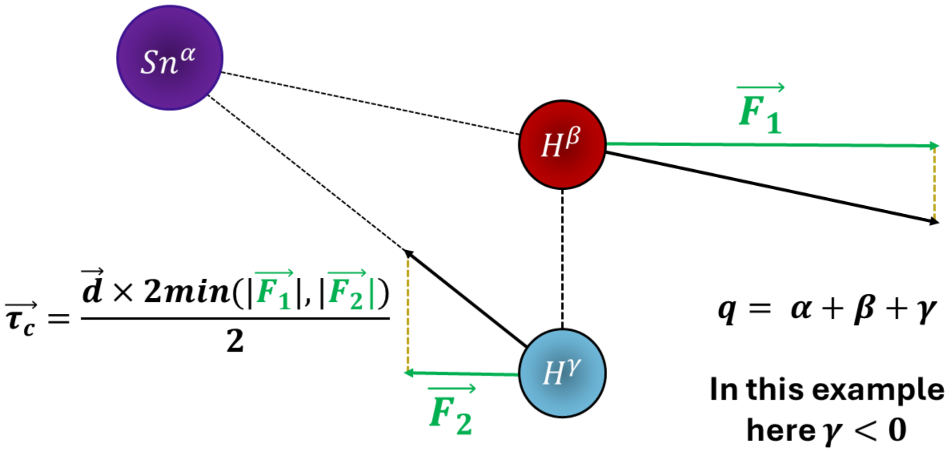

Figure 5: *Force diagram of a polarized* H_2 *near a* Sn^{q+} *ion, showing the force used for a coupled torque calculation.*

In order to get an appropriate force calculation for each hydrogen atom individually a potential needs to be constructed for the interaction of the first hydrogen nucleus with then a fixed tin ion and the second hydrogen nucleus. This seems rather complicated but because we assume a fixed bond length the only interaction force needed to be modeled is between H and Sn. From here a DFT-type potential could still be found and used but the conventional ZBL potential with $Z_1 = 1, Z_2 = 50$ is less complicated to implement and could facilitate finding the order of magnitude of the rotational motion to be expected. If the angular velocity induced is low, the effect of rotational motion might be neglible due to the short interaction window during a collision.

The presence of a charged ion near the hydrogen might also induce a dipole moment, which will lead to a fractional effective charge on each hydrogen atom. As will be shown in section 2.2.5 these fractional occupations can be estimated using density functional theory (DFT). With the effective charge of each atom found, it also might be reasonable to use a Coulomb potential for each individual hydrogen. With this choice the interaction window in which torque is applied to the H_2 is increased as the range of the Coulomb potential is larger than that of the ZBL. In fact the choice of interaction potential is a combination of both because the steep nuclear potential described by a ZBL is still important if inter-nuclear separations get small. The total single hydrogen potential V_H is then:

$$V_H(\mathbf{r}) = \begin{cases} V_c(\mathbf{r}) & \text{if } V_c(\mathbf{r}) - V_{\text{ZBL}}(\mathbf{r}) > 0 \\ V_{\text{ZBL}}(\mathbf{r}) & \text{otherwise,} \end{cases} \tag{9}$$

2.1.3 Stopping Cross-Sections

In GIonS V1 the emphasis of the simulation results was mainly on the average energy loss Sn^{q+} would have per collision with H_2. For GIonS V2 interest has shifted towards the stopping cross-section of Sn^{q+} with respect to H_2. To begin lets define what actually is a stopping power and how it relates to stopping cross-sections. Stopping power is a measure of the energy loss a particle experiences per unit length traversed through a specific medium. If this quantity is then normalized with respect to the density of the material it is known as a stopping cross-section, it is defined in eq (10). Now in this thesis the stopping cross section will be treated in a semi-classical sense [13]. That is, the motions of nuclei are treated with classical dynamics while electrons are described by quantum states.

$$S(E_0) \equiv -\frac{1}{n}\frac{dE}{dx}\bigg|_{E=E_0} \tag{10}$$

Following the description of S it is logical to wonder if there is a direct mathematical operation which could turn average energy losses into stopping cross-sections. The answer is yes but to understand why, first the method used to calculate stopping cross sections will be explained.

Lets imagine a Sn^{q+} ion traversing through a gas of H_2 with density n. As the Sn^{q+} travels a unit distance dx there is a chance that it will collide with a H_2 molecule with some impact parameter b. In that process a set amount of momentum dp is transferred, the exact number is calculated with simulations of GIonS V1 and V2. Momentum transferred is directly related to energy loss but not weighted against the probability of finding a H_2 at impact parameter b within a unit distance dx. The probability of this scenario can be expressed using a differential cross-section as illustrated in figure 6.

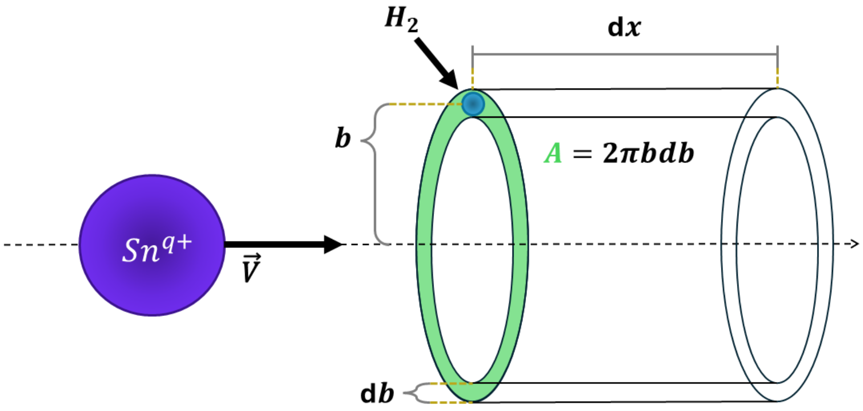

Figure 6: *Differential cross-section of* Sn^{q+} *with a homogeneous gas of* H_2 *molecules.*

Here the idea is that Sn^{q+} will move in a straight line over a short distance dx. The circular symmetry surrounding that path provided the differential cross-section $2\pi bdb$. The unit volume $V = 2\pi bdbdx$ that is then encountered over the time it takes to move dx then corresponds to a number of collisions $N(b)$ through the target density, $N(b) = V \cdot n$. The total expected energy loss over a distance dx is then expressed as:

$$dE = \frac{(dp(E_0, b))^2}{2M_{\text{Sn}}} \cdot 2\pi bdbdx \cdot n \tag{11}$$

Or by using energy loss results directly,

$$dE = \Delta E(E_0, b) \cdot 2\pi bdbdx \cdot n \tag{12}$$

The only thing left to do to find S is reorder equation (12) and add an explicit integral over the impact parameter,

$$-\frac{1}{n}\frac{dE}{dx}\bigg|_{E=E_0} = \int_{b_{min}}^{b_{max}} \Delta E(E_0, b) 2\pi bdb \tag{13}$$

To generalize to collisions with mutliple reaction channels such as electron transfer or excitation an extra weight is added corresponding to the probability of each channel taking place [13],

$$-\frac{1}{n}\frac{dE}{dx}\bigg|_{E=E_0} = \int_{b_{min}}^{b_{max}} \sum_{i=1}^{N} P_i(E_0, b) \cdot \Delta E_i(E_0, b) 2\pi bdb \tag{14}$$

In eq (13), the integration bounds have purposefully left ambiguous. To obtain the theoretically correct result the bounds should be $b_{min} = 0, b_{max} = \infty$, in practice this is not possible due to computation times. Therefore an appropriate choice of b_{max} should be based on a balance of convergence and run time. In the regime the stopping calculations were carried out ($E \in [0.01, 10]$ keV), equation (14) will often be well described by a power law $S(E) \approx \alpha E^{\beta}$. Consequently the characterization of stopping by interaction potential is summarized in what α, β are found to fit this power law the best.

The energy loss function $\Delta E_i(E_0, b)$ found by GIonS V1, was used to calculate the average energy loss $\Delta E_{ave}(E_0)$ one could expect per collision event. In eq (15) the mathematical definition of $\Delta E_{ave}(E_0)$ is given. From these explicit mathematical forms one could notice that $S(E_0)$ and $\Delta E_{ave}(E_0)$ are related up to the normalization used for $\Delta E_{ave}(E_0)$.

$$\begin{aligned}\Delta E_{ave}(E_0) &= \left\langle \sum_{i=0}^{N} P_i(E_0, b) \cdot \Delta E_i(E_0, b) \right\rangle \\ &= \frac{\displaystyle\int_{b_{min}}^{b_{max}} \sum_{i=1}^{N} P_i(E_0, b) \cdot \Delta E_i(E_0, b) 2\pi b db}{\displaystyle\int_{b_{min}}^{b_{max}} 2\pi b db} \\ &= \frac{1}{\pi(b_{max}^2 - b_{min}^2)} \int_0^{b_{max}} \sum_{i=1}^{N} P_i(E_0, b) \cdot \Delta E_i(E_0, b) 2\pi b db\end{aligned} \tag{15}$$

The only thing needed to convert average energy losses to stopping cross-sections is the multiplication by the size of the integration domain. GIonS V1 has used the impact parameter values in atomic units (a_0) after conversion they result in $b_{min} = 0$ a.u. and, $b_{max} = 7.3$ a.u. $\rightarrow \pi b_{max}^2 \approx 5 \cdot 10^{-15} \text{cm}^2$. Previously typical average energy loss values were found to be around $1 - 4$ eV over the whole energy range, multiplying this with πb_{max}^2 results in stopping cross-section of the order $\sim 10^{-14}$ eV cm^2 which matches up well with experimental results such as the Abramenko et al. data [8].

2.2 Density Functional Theory (DFT)

Density Functional Theory (or DFT in short) is a widely used theory for the calculation of electron orbitals in quantum structures ranging from large molecules to crystal structures. The goal of DFT is finding the solutions to the Hamiltonian of a system of interacting electrons by use of a self consistent field (SCF) calculation. In order to do so some approximations and corrections have to be implemented which are of crucial importance to the accuracy of the results coming from DFT. As such, in the coming sections, the need for approximations will be explained. Consequently the necessary corrections will be introduced and discussed.

2.2.1 Formal Framework

The aim of DFT is to find the wave functions of an electronic many-body problem. First we assume that wave-functions of the nuclei and electrons can be treated separately. This approximation is called the Born Oppenheimer approximation [19, 20] and rests on the assumption that due to the relative mass difference between the nucleus and electron, we can think of the nucleus as essentially fixed in the center of mass frame. The presence of the nuclei then only contributes to an external potential $v(\mathbf{r})$ acting on the electrons [21, 19]. Now we define the Schrodinger equation for a system of N interacting non-relativistic electrons.

$$\hat{H}\psi_j(\mathbf{x}_1, \mathbf{x}_2, ..., \mathbf{x}_N) = E_j\psi_j(\mathbf{x}_1, \mathbf{x}_2, ..., \mathbf{x}_N) \tag{16}$$

Where ψ_j refers to the wave function corresponding to j-th energy level of the system. Additionally the Hamiltonian can be divided in to three terms, the kinetic energy operator $\hat{T}$, the potential operator $\hat{V}$ and the electron-electron operator $\hat{W}$.

$$\hat{H} = \hat{T} + \hat{V} + \hat{W} \tag{17}$$

where:

$$\hat{T} = \sum_i^N \frac{-\nabla_i^2}{2} \qquad \hat{V} = \sum_i^N v(\mathbf{r_i})$$

and,

$$\hat{W} = \frac{1}{2}\sum_{i,i\neq j}^N w(|\mathbf{r}_i - \mathbf{r}_j|)$$

Here the $w(\mathbf{r})$ function is any kind of interaction potential between two electrons yet to be specified (an easy example would be the Coulomb potential $w(|\mathbf{r}_1 - \mathbf{r}_2|) = 1/|\mathbf{r}_1 - \mathbf{r}_2|$). Solving the Schrodinger equation for the N-interacting electron system then allows us to find any observable $\mathcal{O}$ by using their operator $\hat{\mathcal{O}}$ on the solution's wavefunctions:

$$\mathcal{O}_j = \langle\psi_j|\, \hat{\mathcal{O}}\, |\psi_j\rangle \tag{18}$$

While the definition of the many body system appears rather straightforward, solving (16) in analytical terms becomes impossible for larger systems. In order to still advance and obtain a workable solution we have to turn to approximations and numerical methods. There are many possible ways the many body problem has been tackled historically, examples include Hartree-Fock (HF) theory, diagrammatic Green's function techniques, Monte Carlo (MC) approaches and Configuration Interaction (CI) expansions [19]. In this thesis the choice was made to explore and use a higher order version of Hartree-Fock theory, called Density Functional Theory (DFT).

The first step to understanding Hartree-fock, and by extension DFT, is to shift from electron wave functions to electron densities. Lets assume we are able to find the groundstate wave-functions of N interacting electrons. In that case the probability of finding an electron at $\mathbf{r}$ can be expressed by the so called electron density $n(\mathbf{r})$ [19].

$$n_0(\mathbf{r}) = N \int d\mathbf{x}_2 \cdots \int d\mathbf{x}_N |\psi_0(\mathbf{r}, \mathbf{x}_2, \ldots, \mathbf{x}_N)|^2 \tag{19}$$

As the wave-function used to calculate $n_0(\mathbf{r})$ is obtained from the Schrodinger equation, and that itself is dependent on $v(r)$, we can write the ground state electron density as a functional of $v(r)$ like, $n_0[v](\mathbf{r})$. Next we need to consider if the inverse is also true, is the external potential a functional of $n_0(\mathbf{r})$? The question is answered in the Hohenberg-Kohn theorem which states:

Hohenberg-Kohn theorem. In a finite, interacting electron system with a given particle-particle interaction there exists a one-to-one correspondence between the external potential $v(\mathbf{r})$ and the ground-state density $n_0(\mathbf{r})$. In other words, the external potential is a unique functional of the ground-state density, $v[n_0](\mathbf{r})$, up to an arbitrary additive constant. [19, 22]

The full proof of the Hohenberg-Kohn theorem is given in [19, 22]. This theorem has the important implication that two ground state wave functions that differ up to more than a phase factor produce two unique ground state electron densities. This allows us to state that any mapping from $\psi_0 \to n_0$ is one to one, and by extension that the wave-functions are functionals of the electron density, $\psi_0[n_0](\mathbf{r})$. Additionally we can also write $\hat{V}[n_0]$ and because $\hat{T}$ and $\hat{W}$ do not involve any potential term they are fixed. Furthermore it means that the Hamiltonian is also a functional of n_0. By now substituting $\hat{H}[n_0]$ into the Schrodinger equation (16), it should be evident that all eigenstates of the Hamiltonian are electron density functionals $\psi_j[n_0]$, in addition to the ground state ψ_0. Note that explicitly ψ_j is a functional of the ground state density n_0[1]

Additionally in Hohenberg-Kohn's original paper [22] it is shown that for a potential v_0 the total energy functional $E_{v_0}[n] > E_0$ if $n \neq n_0$ and $E_{v_0}[n] = E_0$ if $n = n_0$ [19, 22]. The total energy functional is defined as:

$$E_{v_0}[n] = \langle \psi[n] | \hat{T} + \hat{V}_0 + \hat{W} | \psi[n] \rangle \tag{20}$$

By finding a minimum in $E_{v_0}[n]$, n_0 could theoretically be found. By making use of the method of Lagrange multipliers this statement is translated in a very useful property seen in eq (21). Here μ denotes the Lagrange multiplier ensuring a set number of electrons is in the system. See section 2.2.6 for a basic explanation of the method of Lagrange multipliers and for a more in depth look at how this expression is obtained.

$$\frac{\delta}{\delta n(\mathbf{r})} \left[E_{v0}[n](\mathbf{r}) - \mu \int d^3r' n(\mathbf{r}') \right] = 0 \tag{21}$$

Equation (21) is referred to as the DFT Lagrange equation and holds for any system with or without the inclusion of electron-electron interactions. However finding n_0 through this method is not feasible as $\hat{W}$ is often unknown, for that reason a different formalism is needed which was proposed by Kohn and Sham in 1965 [26].

---

[1] This result is reproduced in a theory within DFT which calculates excited state energies of systems named, linear response theory [23]. Linear response theory is a branch of time dependent density functional theory (TDDFT) [23, 24, 25] and has a generalized version of the Hohenberg-Kohn theorem called the van Leeuwen theorem [24].

The main result of the formal frame work of these density functionals and operators is that in order to find the total energy of a system we do not have to solve the Schrodinger equation. Instead finding the electron density of the system is an equally valid option which in theory should lead to the same answers. In practice finding the ground-state density is not straight forward and involves the introduction of a self-consistent field (SCF) calculation [19, 21, 27]. This solving method is the next topic.

2.2.2 Kohn Sham equations

To obtain the famous Kohn Sham equations we start by considering the many body problem with a Hamiltonian but now we omit the self interaction of electrons, i.e. we remove the electron-electron operator $\hat{W}$. This simplification turns our many body problem into a non interacting many body problem. The motivation behind it is to make it easier to solve the electron orbitals while introducing an interaction potential that does attempt to remedy the lack of an e-e interaction term in the Hamiltonian.

First lets start off by explicitly writing the Kohn Sham Hamiltonian [19]:

$$\hat{H}_s = \hat{T} + \hat{V}_s = \sum_{i=1}^{N} \left(-\frac{\nabla_i^2}{2} + v_s(\mathbf{r}_i) \right) \tag{22}$$

Here, $\hat{V}_s$ and v_s refer explicitly to the yet to be determined potential that corrects for e-e interactions. Due to the omission of electron-electron terms we can actually turn the Schrodinger equation (16) into a set of independent differential equations (23) [19].

$$\left[-\frac{1}{2}\nabla^2 + v_s[n](\mathbf{r}) \right] \phi_i(\mathbf{r}) = E_i \phi_i(\mathbf{r}) \tag{23}$$

With all of the single electron wave functions ϕ_i we can find the total electron wave-function. In order to abide by Pauli's exclusion principle the total wave-function is given by a single Slater determinant:

$$\psi_s(\mathbf{r}_1, \ldots, \mathbf{r}_N) = \frac{1}{\sqrt{N!}} \begin{vmatrix} \phi_1(\mathbf{r}_1) & \phi_2(\mathbf{r}_1) & \ldots & \phi_N(\mathbf{r}_1) \\ \phi_1(\mathbf{r}_2) & \phi_2(\mathbf{r}_2) & \ldots & \phi_N(\mathbf{r}_2) \\ \vdots & \vdots & \ddots & \vdots \\ \phi_1(\mathbf{r}_N) & \phi_2(\mathbf{r}_N) & \ldots & \phi_N(\mathbf{r}_N) \end{vmatrix} \tag{24}$$

which is automatically anti-symmetric under electron exchange as required [19, 20, 28]. With this total wave function one could once again obtain the electron density using equation (19). However an alternative equation (25) can also be used provided the calculated orbitals are orthogonal.

$$n(\mathbf{r}) = \sum_{i=1}^{N} \langle \phi_i(\mathbf{r}) | \phi_i(\mathbf{r}) \rangle \tag{25}$$

The orthogonality condition is not trivially present in the set of ϕ_i's but in most cases the set of orbitals can be orthogonalized [20], this process will be discussed in section 2.2.3.

The total energy functional is defined as:

$$E_{v_0}[n] = F[n] + \int dr^3 n(\mathbf{r}) v_0(\mathbf{r}) \tag{26}$$

Where $F[n] = T[n] + W[n] = T_s[n]$ and $v_0 = v_s$ in the non interacting case. Now we transform the non-interaction picture into one with an effective single-particle picture by writing:

$$E_{v_0}[n] = T_s[n] + \int d^3 r n(\mathbf{r}) v(\mathbf{r}) + \frac{1}{2} \int d^3 r \int d^3 r' \frac{n(\mathbf{r}) n(\mathbf{r}')}{|\mathbf{r} - \mathbf{r}'|} + E_{xc}[n] \tag{27}$$

where the E_{xc} is called the exchange-correlation energy [19, 21]. E_{xc} is a rather important quantity as it heavily influences what the effective potential will look like. With that in mind a well informed choice of exchange correlation functional should be made and thus it will be discussed in more detail in section 2.2.4. We can also substitute in the Coulomb/Hartree energy $E_H[n]$ [19] which is defined as:

$$E_H[n] = \frac{1}{2} \int d^3 r \int d^3 r' \frac{n(\mathbf{r}) n(\mathbf{r}')}{|\mathbf{r} - \mathbf{r}'|} \tag{28}$$

With a total energy functional expression for both type of interaction pictures we work out the DFT Lagrange equation (21) for both systems:

$$\frac{\delta E_{v_0}[n]}{\delta n(\mathbf{r})} = \frac{\delta T_s[n]}{\delta n(\mathbf{r})} + v_0(\mathbf{r}) + \int d^3 r' \frac{n(\mathbf{r}')}{|\mathbf{r} - \mathbf{r}'|} + \frac{\delta E_{xc}}{\delta n(\mathbf{r})} = \mu$$

$$\frac{\delta E_{v_s}[n]}{\delta n(\mathbf{r})} = \frac{\delta T_s[n]}{\delta n(\mathbf{r})} + v_s(\mathbf{r}) = \mu \tag{29}$$

By now setting $\frac{\delta E_{v_0}[n]}{\delta n(\mathbf{r})} = \frac{\delta E_{v_s}[n]}{\delta n(\mathbf{r})}$ we are conceptually equating a non-interacting system with some effective potential $v_s(\mathbf{r})$ to a system with electron-electron interactions and the potential created by atoms $v_0(\mathbf{r})$. If we do this and solve for $v_s(\mathbf{r})$ we get:

$$v_s[n](\mathbf{r}) = v_0(\mathbf{r}) + \int d^3 r' \frac{n(\mathbf{r}')}{|\mathbf{r} - \mathbf{r}'|} + \frac{\delta E_{xc}}{\delta n(\mathbf{r})} \tag{30}$$

with $v_{xc}[n](\mathbf{r}) \equiv \frac{\delta E_{xc}}{\delta n(\mathbf{r})}$. Finding the full expression of $v_s[n](\mathbf{r})$ will allow us to find the ground-state electron density by solving (23).

In the DFT solving method no spin was mentioned thus far. By partitioning the total electron density into a spin up and spin down part we can actually generalize the previous equations to include spin effects [19].

$$N = N_\uparrow + N_\downarrow \iff n_j(\mathbf{r}) = n_{j,\uparrow}(\mathbf{r}) + n_{j,\downarrow}(\mathbf{r}) = \sum_{\sigma=\uparrow,\downarrow} \sum_{i=1}^{N_\sigma} \langle \phi_{i,\sigma} | \phi_{i,\sigma} \rangle$$

The partitioning also has minor effect on the functionals, which are now a functional of both $n_\uparrow(\mathbf{r})$ and $n_\downarrow(\mathbf{r})$:

$$\left[-\frac{1}{2} \nabla^2 + v_{s,\sigma}[n_\uparrow, n_\downarrow](\mathbf{r}) \right] \phi_{i,\sigma}(\mathbf{r}) = E_{i,\sigma} \phi_{i,\sigma}(\mathbf{r}) \tag{31}$$

$$v_{s,\sigma}[n_\uparrow, n_\downarrow](\mathbf{r}) = v_0(\mathbf{r}) + \int d^3 r' \frac{n_\uparrow(\mathbf{r}') + n_\downarrow(\mathbf{r}')}{|\mathbf{r} - \mathbf{r}'|} + v_{xc,\sigma}[n_\uparrow, n_\downarrow](\mathbf{r}) \tag{32}$$

Note that now we do not seek an expression or approximation of $E_{xc}[n]$ but rather $E_{xc}[n_\uparrow, n_\downarrow]$. Because an electron density is needed as input in both the normal (30) and spin resolved (32) effective potentials, there is a need for an initial guess of $n(\mathbf{r})$. With the potential resulting from this guess we will get a new electron density through eq (31), which is likely very different from the initial guess. So we repeat the process, now finding $v_s[n]$ with the new $n(\mathbf{r})$ as a more educated guess. In principle this process should be repeated until there is no change in $n(\mathbf{r})$, yet often the energy difference between iterations could be of the order of fractions of eV's after 10-40 iterations (depending on the problem at hand). Instead convergence criteria are implemented often involve quantities like the norm of the orbital gradient as is the case in quantum chemistry package NWChem[15].

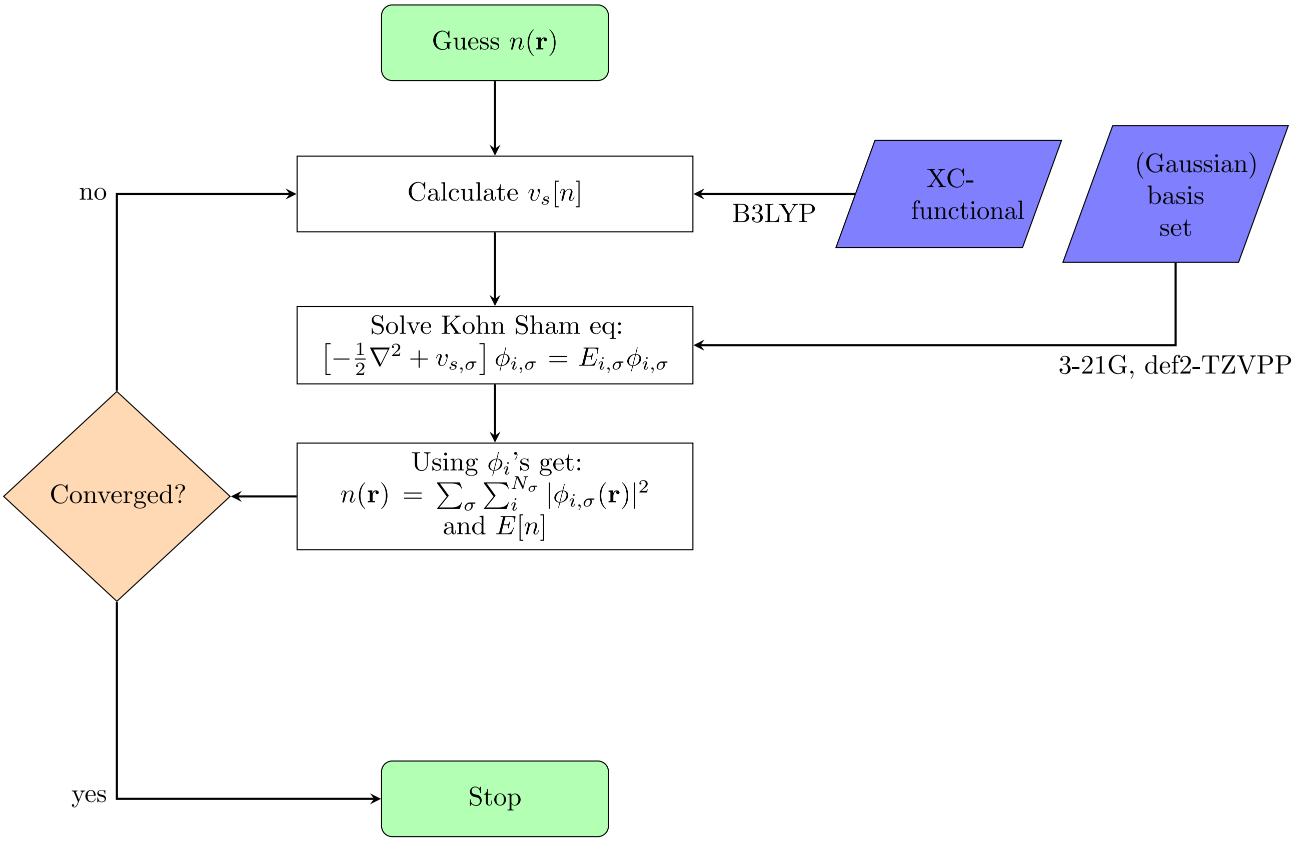

Figure 7: *Flow chart of the iterative self consistent field procedure in DFT.*

This SCF iterative method (schematically illustrated in figure 7) is a very powerful result, only undercut by a poor choice of basis set and exchange-correlation (xc) functional $E_{xc}[n]$. Choosing the right functional can be a difficult task, that is why section (2.2.4) has been dedicated to explaining the different types and their advantages and shortcomings. The same holds for the choice of basis set, which will be discussed now.

2.2.3 Basis sets

With the general ideas laid out in the previous section it should now be somewhat clear what DFT is. One thing that was skimmed over, is finding solution to the Kohn-Sham equations (31). In highly symmetric systems solutions may be found analytically [19, 21], yet in most applications in DFT we are forced to seek a numerical approach. Because we are dealing with a linear 2nd order differential equation it is actually possible to use a superposition of states to construct a viable solution. This property is efficiently exploited by DFT by supplying its solving method with so called basis functions [21]. Basis functions are usually common occurring orbitals and a set of them is referred to as a basis set. Because basis functions are themselves a solution to a Schrodinger equation (albeit with a different interaction potential), they can be thought of as vectors living in their own vector space called Hilbert-space. A the set of these vectors then span a subspace of Hilbert-space, which corresponds to a set of solutions we can find to the Kohn-Sham equations. This argument supports the probable notion that the size of the basis set used for a DFT calculation is rather important to obtaining meaningful results.

Basis sets are often ordered according to the number of independent basis functions per occupied valence orbital also called cardinal number [21]. Having a basis set with high cardinal number is in some cases crucial to form electron orbitals that encompass the fine details needed for the problem at hand. In any application of DFT we are resorted to using a finite set of these basis functions. By using a restricted set of function, new possible sources of error are introduced in the computation of orbitals. The first is the basis set incompleteness error (BSIE) [21] which occurs when your basis functions do not span a sufficient function space to describe the solution to the Kohn-Sham equations. A valid way to probe the presence and magnitude of BSIE is by evaluating your DFT calculation with both a basis set with a set cardinal number and a higher cardinal number, and looking at the difference.

The other type of common occurring error is a basis set super position error (BSSE) [21, 29]. BSSE is a phenomenon where basis set functions of different nuclei start to overlap which usually happens at close nuclei separations. The overlap of these basis functions increases the set size of nearby nuclei which could end up lowering the total energy of the system found if the initial basis set used is small. BSSE is a particular issue if a geometry optimization over some internal coordinate is carried out. An example of this is an optimization trying to find the bond length of diatomic molecules that correspond to a minimum in the energy, in other words calculating the optimal bond length. Because of the BSSE effect, shorter separations are actually favoured for energy optimization causing a deviation in the bond length of fractions of angstroms. In this project no geometry optimizations were carried out as instead tabulated NIST values [18] for H_2 were used. Though this limits the effect BSSE would have, a basis set that is too small could still skew the potential energy function found by DFT.

As stated prior, finding the electron density from orbitals can be done efficiently if the orbitals are orthogonal. For two electrons, one occupying the $\phi_\nu(\mathbf{r})$ orbital and one occupying the $\phi_\mu(\mathbf{r})$ orbital, this condition can be put into mathematical terms [20]:

$$\int d^3r\phi^*_\mu(\mathbf{r})\phi_\nu(\mathbf{r}) = \delta_{\mu\nu} \tag{33}$$

But if there is linear dependence within the set of orbitals, the right hand side contains off-diagonal elements:

$$\int d^3r\phi^*_\mu(\mathbf{r})\phi_\nu(\mathbf{r}) = \mathbf{S}_{\mu\nu} \tag{34}$$

Given this matrix $\mathbf{S}_{\mu\nu}$ there are two general procedures to orthogonalize the electron orbitals through a basis transformation. For an undisclosed transformation matrix $\mathbf{X}$ we write a set of N orthogonal orbitals ϕ':

$$\phi'_\mu = \sum_{\nu}^{N} \mathbf{X}_{\nu\mu}\phi_\nu \qquad \mu = 1, 2, \cdots, N \tag{35}$$

where the requirement is that $\mathbf{X}$ transforms the set such that:

$$\int d^3r\phi'^*_\mu(\mathbf{r})\phi'_\nu(\mathbf{r}) = \delta_{\mu\nu}. \tag{36}$$

By using equations (35) and (34) in eq (36) it can be shown that $\mathbf{X}$ has the property:

$$\mathbf{X}^\dagger\mathbf{S}\mathbf{X} = \mathbb{1} \tag{37}$$

Additionally $\mathbf{S}$ is Hermitian, meaning it can be diagonalized with a unitary matrix $\mathbf{U}$:

$$\mathbf{U}^\dagger\mathbf{S}\mathbf{U} = \mathbf{s} \tag{38}$$

Here we have found a set of equations for the elements in $\mathbf{X}$. The first option for orthogonalization method is called symmetric orthogonalization [20] which uses:

$$\mathbf{X} \equiv \mathbf{U}\mathbf{s}^{-\frac{1}{2}}\mathbf{U}^\dagger, \tag{39}$$

and has the distinct disadvantage of blowing up in the case of small linear dependencies in the orbital set. Here for some μ, $\mathbf{s}_\mu$ will be close to zero thus leading to the division of a small number in (39). The other method is called canonical orthoginalization [20] and chooses:

$$\mathbf{X} = \mathbf{U}\mathbf{s}^{-\frac{1}{2}}, \tag{40}$$

Initially it seems the same division problem might occur here as well. Nevertheless, in canonical orthoginalization there is a remedy to eliminate the small linear dependencies. For the sake of argument lets say there are m small linear dependencies. First we start by orderding the eigenvalues $\mathbf{s}$ in terms of magnitude. Subsequently the m problematic eigenvalues are truncated from s and at the same time $\mathbf{X}$, resulting in a new transformation matrix:

$$\tilde{\mathbf{X}} = \begin{bmatrix} \frac{U_{11}}{s_1} & \frac{U_{12}}{s_2} & \cdots & \frac{U_{1N'}}{s_{N'}} \\ \frac{U_{21}}{s_1} & \frac{U_{22}}{s_2} & \cdots & \frac{U_{2N'}}{s_{N'}} \\ \vdots & \vdots & \ddots & \vdots \\ \frac{U_{N1}}{s_1} & \frac{U_{N2}}{s_2} & \cdots & \frac{U_{NN'}}{s_{N'}} \end{bmatrix} \quad \text{with} \quad N' = N - m \tag{41}$$

Effectively we have shrunk the size of the basis set from N to $N - m$ functions[2]. The new orbitals are given in eq (41):

$$\phi'_\mu = \sum_\nu^N \tilde{\mathbf{X}}_{\nu\mu}\phi_\nu \qquad \mu = 1, 2, \cdots, N - m \tag{42}$$

2.2.4 Exchange Correlation Functionals

The strength of the formal framework set out by Kohn and Sham is the formally exact way it treats many-particle correlation and fermionic exchange effects [19]. At the heart of this exact approach is the $E_{xc}[n(\mathbf{r})]$ which in reality is not exact and prone to self-interaction-errors (SIEs). One of the challenges of the Kohn-Sham DFT formalism is obtaining a good analytical description of the exchange correlation (xc) functional. Over the years, many xc-functionals have been developed, to understand the need of some improvements lets first have a look at the desired characteristics of a good xc-functional.

A well behaved xc-functional has two equivalent properties:

---

[2] Note that the Hartree-fock energy (introduced in the next section) can be re-evaluated after finding the transformation by using the transformation matrix $\tilde{\mathbf{X}}$ directly instead of repeating the whole calculation with the new set of orbitals.

Exchange Correlation Functionals: A xc-functional must not contain any self interaction. This requirement translates to a condition: $E_H[n_{j,\sigma}] + E_{xc}[n_{j,\sigma}, 0] = 0$. Each orbitals self-Hartree energy must be cancelled by its xc-energy.

$\Longleftrightarrow$

The xc-potential should behave like $v_{xc}(\mathbf{r}) \to -\frac{1}{|\mathbf{r}|}$ as $|\mathbf{r}| \to \infty$

Usually the xc-functional is split up into two parts, the exchange energy and correlation energy functional. An exact expression for the exchange energy density in terms of orbitals exists and is given by [19, 21]:

$$e_x^{\mathrm{HF}}(\mathbf{r}) = -\frac{1}{2}\sum_{\sigma}\sum_{i,j=1}^{N_\sigma}\int d^3r'\,\frac{\phi^*_{i,\sigma}(\mathbf{r}')\phi_{j,\sigma}(\mathbf{r}')\phi_{i,\sigma}(\mathbf{r})\phi^*_{j,\sigma}(\mathbf{r})}{|\mathbf{r}-\mathbf{r}'|} \quad , \quad E_x^{\mathrm{HF}} = \int d^3r\, e_x^{\mathrm{HF}}(\mathbf{r}) \tag{43}$$

The exact exchange energy is usually referred to as the Fock or Hartree Fock (HF) exchange energy. Note however that this expression is not an explicit functional of $n(\mathbf{r})$ (only implicit through the orbitals). This poses a practical problem as taking a functional derivative with respect to $n(\mathbf{r})$ is impossible analytically, meaning there is not a full expression for $v_{xc}(\mathbf{r})$. Yet, e^{HF} is still used in higher order approximations as we will see shortly.

Without the exact formulation, functionals need to rely upon empirical data of chemical properties and subsequently the fitting of proposed models. The first functional that was formed by Kohn and Sham [19, 26] is called the Local Spin Density Approximation (LSDA). This method uses theoretical results of a homogeneous electron liquid with (constant over space) density n' for the exchange energy density, $e_x^h(n'_\uparrow, n'_\downarrow)$. Additionally the correlation density $e_c^h(n'_\uparrow, n'_\downarrow)$ has been analytically parameterized based off highly precise electron liquid simulation results. The total energy xc-energy density $e_{xc}^h(n'_\uparrow, n'_\downarrow) = e_x^h(n'_\uparrow, n'_\downarrow) + e_c^h(n'_\uparrow, n'_\downarrow)$ is then used to express the xc-functional as a simple integral:

$$E_{xc}^{\mathrm{LSDA}}[n_\uparrow, n_\downarrow] = \int d^3r\, e_{xc}^h(n_\uparrow(\mathbf{r}), n_\downarrow(\mathbf{r})) \tag{44}$$

and the LDA potential:

$$v_{xc}^{\mathrm{LSDA}}(\mathbf{r}) = \left.\frac{de_{xc}^h(n'_\uparrow, n'_\downarrow)}{dn'_\sigma}\right|_{n'_\sigma = n_\sigma(\mathbf{r})} \tag{45}$$

From these expressions it becomes clear why this is called a ”local density approximation” of the xc-functional. The energy contribution provided by this functional at position $\mathbf{r}_0$ corresponds to the energy gained if an electron density $n(\mathbf{r_0})$ is present at $\mathbf{r}_0$ with a $n(\mathbf{r}_0)$ dense homogeneous electron liquid surrounding it. We can also infer from this that the LSDA-functionals are a good attempt at describing the xc-energies in cases with a high level of homogeneity in the electron density but start to lack cases with strong gradients in $n(\mathbf{r})$. This suspicion is matched in reality as LSDA's often include self interaction and faulty asymptotic behaviour [19, 30], $v_{xc}(\mathbf{r}) \to -e^{-\alpha|\mathbf{r}|}$ as $|\mathbf{r}| \to \infty$.

The LSDA is an approximation of the first order (also called rung). To improve upon it, the next logical step would be to factor in a changing local gradient. The collection of the xc-functionals that realize this is called, the Generalized Gradient Approximations (GGA) and these are of the second rung. There are many different forms of GGA but a popular one is ”BLYP” which consist of an exchange functional by Becke: B88 [31] and a correlation functional by Lee, Yang and Parr: LYP [32]. Many of these functionals require the fitting of function parameters for the model, in the case of the Becke functional it is done by fitting to atomic Hartree-Fock exchange energies. Another xc-functionals PBE [33], was developed by John Perdew et al., where noteably the parameter fitting was done non-empirically and instead focused on getting a well behaved functional [19].

There are also approximations of the third-rung called meta-GGA's. The functionals of this type include laplacians of the electron density and Kohn-Sham orbital kinetic energy densities as variables of the xc-energy density and xc-potential. The main improvement of the meta-GGA's is the partial alleviation of self-interaction which was often a problem in the conventional second rung GGA's [19, 30]. These higher order functionals are not without their limitations however, the kinetic-energy density is merely an implicit functional of the electron density leading to problems evaluating the xc-potential. Historically a formal method was developed within DFT to still evaluate v_{xc}, with a downside being more computationally expensive.

At the fourth rung we have hybrid functionals, these are comprised out of a mix of the exact exchange energy functional (seen in (43)) and a combination of LDA's and GGA's [19]. As stated with the meta-GGA's there are ways to actually evaluate v_{xc} even with the presence of implicit functionals in E_{xc} as with E_{xc}^{HF}. A widely used hybrid is the B3LYP functional [31, 32, 34], which is given by:

$$E_{xc}^{\mathrm{B3LYP}} = (1-a)E_x^{\mathrm{LDA}} + aE_x^{\mathrm{HF}} + b\Delta E_x^{\mathrm{B88}} + cE_c^{\mathrm{LYP}} + (1-c)E_c^{\mathrm{LDA}} \tag{46}$$

with: $a = 0.20$, $b = 0.72$, $c = 0.81$ and $\Delta E_x^{\mathrm{B88}}$ is Becke's 1988 gradient correction for exchange. B3LYP has been shown to reproduce structural and energetic properties of molecules more accurately than most (meta) GGAs, hence its popularity. Nevertheless, the asymptotic behaviour of even the popular B3LYP is incorrect [35], $v_{xc}(\mathbf{r}) \to -\frac{0.2}{|\mathbf{r}|}$ as $|\mathbf{r}| \to \infty$.

From a theoretical perspective all SIEs can be attributed to the incorrect description of regions near a molecule with effective fractional charges [19, 35]. Range-separated hybrid functionals (RSHs) were created to effectively counter the SIE by partitioning the use of approximate functionals and the Hartree Fock exchange over inter-electronic distances $r_{12} = |\mathbf{r}_1 - \mathbf{r}_2|$. The goal is to obtain asymptotically correct behaviour by using Hartree Fock exchange in the far limit while close by a normal hybrid functional is sufficient (and less expensive to run).

The way these range separated functionals are constructed is by first using a Ewald split where a parameterization called the Coulomb attenuated method (CAM) [35, 36] is used (see eq (47)). Here we split the Coulomb potential into two parts, each of which will use a different xc-functional to calculate the total xc-energy.

$$\frac{1}{r_{12}} = \frac{\alpha + \beta \operatorname{erf} \mu r_{12}}{r_{12}} + \frac{1 - (\alpha + \beta \operatorname{erf} \mu r_{12})}{r_{12}} \tag{47}$$

In eq (47) the first term becomes dominant at long ranges and the second at short ranges. We then split the exchange functional up into a long range and short range contribution, $E_x = E_x^{\mathrm{LR}} + E_x^{SR}$. By picking the first term of (47) and once again working out the exact exchange functional in terms of orbitals, we find [35]:

$$\begin{aligned} E_x^{\mathrm{LR}} &= \alpha E_x^{\mathrm{HF}} - \frac{\beta}{2} \sum_\sigma \sum_{i,j=1}^{N_\sigma} \int d^3 r_1 \int d^3 r_2 \phi_{i,\sigma}^*(\mathbf{r}_1)\phi_{j,\sigma}(\mathbf{r}_1) \frac{\operatorname{erf} \mu r_{12}}{r_{12}} \phi_{i,\sigma}(\mathbf{r}_2)\phi_{j,\sigma}^*(\mathbf{r}_2) \\ &= \alpha E_x^{\mathrm{HF}} + \beta E_x^{\mathrm{LR,HF}} \end{aligned} \tag{48}$$

In this expression we can interpret erf μr_{12} as a weight function. In the domain of space where $r_{12} \ll 1/\mu$, the energy density $E_x^{\mathrm{LR}}(\mathbf{r}) \approx \alpha E_x^{\mathrm{HF}}(\mathbf{r})$ and where $r_{12} \gg 1/\mu$, $E_x^{\mathrm{LR}}(\mathbf{r}) \approx (\alpha+\beta) E_x^{\mathrm{HF}}(\mathbf{r})$. We can clearly see here how the partitioning of the Coulomb force results in two different contributions to the total xc-energy for different ranges. In a similar manner the short range term in (47) will enter into the expression of the LDA's and (meta)-GGA's total exchange energy. An example of a RSH is CAM-B3LYP [35]:

$$\begin{aligned} E_{xc}^{\text{CAM-B3LYP}} =& \alpha E_x^{\mathrm{HF}} + (1-\alpha) E_x^{\mathrm{Slater}} + \gamma \Delta E_x^{\mathrm{B88}} \\ &+ \beta(E_x^{\mathrm{LR,HF}} - E_x^{LR,\mathrm{B88}}) + \delta E_c^{\mathrm{LYP}} + \epsilon E_c^{\mathrm{VWN(5)}} \end{aligned} \tag{49}$$

With $\alpha = 0.19$, $\beta = 0.46$, $\gamma = 0.81$, $\delta = 0.81$, $\epsilon = 0.19$, and $\mu = 0.33$.

The fifth and highest rung of xc-functional is made up out of double hybrid functionals. The major improvement over the lower rung functionals is the inclusion of unoccupied orbitals in the correlation functionals [19]. To do so an expansion for the exact correlation energy in terms of higher order many-body pertubation terms is used. Not a lot of these functionals exist as of today, a few standard examples being: B2PLYP, B2GP-PLYP and PWPB95 [19]. These functionals all calculate the correlation up to second order perturbative level (MP2). Doing so comes at a cost, as typically the computational load is roughly twice that of the conventional B3LYP [19].

2.2.5 Space Partitioning / Population Analysis

For general gradient approximation (GGA) type functional (and PBE in particular) another type of partitioning is sometimes used, called a quasi-non-uniform gradient-level approximation (QNA) [37]. In metal lattices, GGA's main source of errors come from a gradient sensitive area near the nuclei. In order to optimize the performance of the xc-functional the model parameters need to be changed in these error-prone regions. For an efficient way of treating this the total integration domain needs to be partitioned into cells, each corresponding to an individual nucleus. If the cell corresponding to atom i is denoted as Ω_i then the QNA xc-functional can be mathematically defined as,

$$E_{xc}^{\mathrm{QNA}}[n] = \sum_i \int_{\Omega_i} d^3 r e_x^{\mathrm{LDA}}[n] F_{xc,i}^{\mathrm{opt}}[n] \tag{50}$$

Here $F_{xc,i}^{\mathrm{opt}}$ refers to the optimalization function which varies mixing parameters within the GGA. These are GGA dependent and do not take a general form. The xc-functional in eq (50) was introduced as a valid motivation to explain Becke's space partitioning method [38] as it affects the xc-functional significantly. To simplify the description of the problem we replace the integration domain Ω_i by yet to be determined weight function w_i that drops at the domain boundaries. With that the partitioning problem can be reduced to its essential form, we have an integral I with some integrand $F(\mathbf{r})$ partitioned into N pieces, see eq (51). Now the focus lies on finding a weight function that is easily constructed from any geometry and yields reasonable results with experimental values.

$$I = \int d^3 r F(\mathbf{r}) = \sum_{n=1}^{N} \int d^3 r F_i(\mathbf{r}) w_i(\mathbf{r}) \tag{51}$$

We are interested in ways to partition the volume around atomic centers, for this Becke proposed a general efficient method. The theory starts with the observation that for any 3D-space a unique polyhedron can be coupled to each nucleus, to that effect filling the entire space. These can be constructed by finding all perpendicular bisecting planes corresponding to all vectors $R_{i,j}$ joining nucleus i to j. The set of polyhedra is referred to as Voronoi polyhedra or Voronoi cells[3][38], their formulation can be carried out for any distribution of nuclei, a 2D example is given in figure 8.

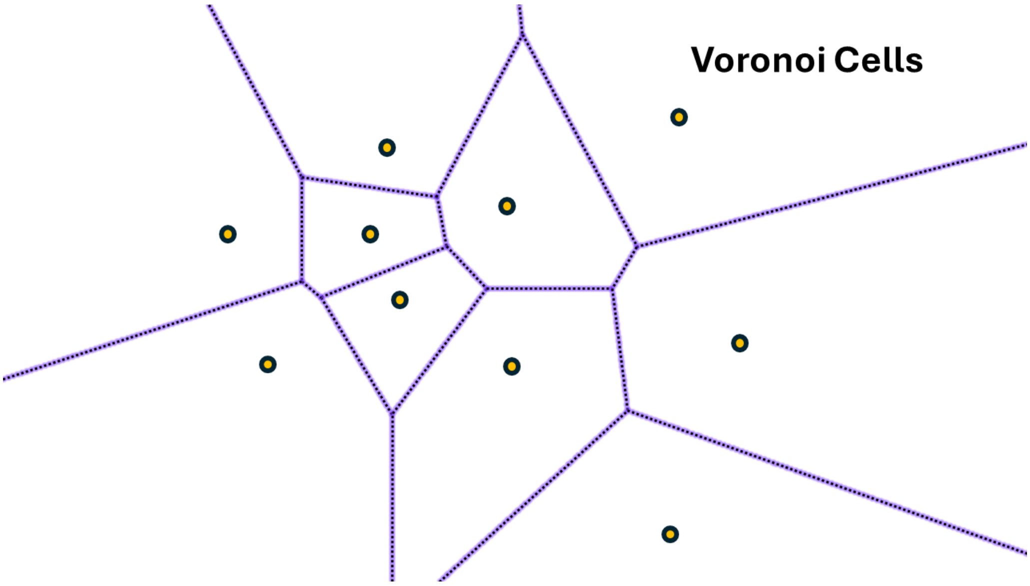

Figure 8: *Schematic of a set of Voronoi cells. For a homogeneous material with nuclei depicted as the yellow dots, this is also the set of cell created by Becke's partitioning method.*

For this procedure a coordinate switch is made, for any two atoms in the system we define the confocal elliptical coordinates (λ, μ, θ)[4] with $\lambda \in [1, \infty)$, $\mu \in [-1, 1]$, and $\theta \in [-\pi, \pi]$. For atoms i and j these coordinates are given by:

$$\lambda_{i,j} = \frac{|\mathbf{r_i}| + |\mathbf{r_j}|}{R_{i,j}} \qquad \mu_{i,j} = \frac{|\mathbf{r_i}| - |\mathbf{r_j}|}{R_{i,j}} \tag{52}$$

which immediately illustrates the reason for this coordinate choice. Lets take for an example a diatomic molecule like H_2. For H_2 any point $(x_0, y_0, z_0) \rightarrow (\lambda_0, \mu_0, \theta_0)$ is closer to nucleus i if $\mu_{i,j} > 0$ and closer to j if $\mu_{i,j} < 0$. In the case that a diatomic molecule is homonuclear, we can assume that the sphere of influence of both the nuclei is the same. This means that if we have two similar nuclei i and j the choice of weight function $w_i \equiv \omega_{i,j}$ for assigning electron density to atom i can be made using a heaviside step function [38]:

$$\omega_{i,j}(\mathbf{r}) = \begin{cases} 1 & \text{if } -1 \leq \mu_{i,j} \leq 0, \\ 0 & \text{if } 0 < \mu_{i,j} \leq 1, \end{cases} \tag{53}$$

If more of the same nuclei are added into the total system this generalizes to:

$$w_i(\mathbf{r}) = \prod_{j \neq i} \omega_{i,j}(\mathbf{r}). \tag{54}$$

---

[3] Also known as Wigner-Seitz cells if dealing with a periodic lattice.

[4] For a vector in elliptical coordinates connecting the origin to a point, θ refers to the angle to the inter nuclear axis, λ to ellipses with foci at the nuclei positions and μ to hyperboloids.

which is then consequently also the definition of the Voronoi polyhedron associated to nucleus i. This argumentation is reasonable for a system of only one type of nuclei, but how about a hetero nuclear system? Becke proposes a change taking into account differing atomic sizes by shifting the division line according to the ratio of the Bragg-Slater radii $\chi = \frac{R_i}{R_j}$ [38].

$$v_{i,j} = \mu_{i,j} + a_{i,j}(1 - \mu_{i,j}^2) \tag{55}$$

$$a_{i,j} = \frac{u_{i,j}}{u_{i,j}^2 - 1} \ \ , \ \ u_{i,j} = \frac{\chi - 1}{\chi + 1} \tag{56}$$

where now,

$$\tilde{\omega}_{i,j}(\mathbf{r}) = \begin{cases} 1 & \text{if } v_{i,j} > 0, \\ 0 & \text{if } v_{i,j} < 0, \end{cases} \tag{57}$$

which once again generalizes the Voronoi polyhedron to a product:

$$w_i(\mathbf{r}) = \prod_{j \neq i} \tilde{\omega}_{i,j}(\mathbf{r}). \tag{58}$$

Note that if $\chi > 2.4$ then $a_{i,j} > \frac{1}{2}$ meaning setting $v_{i,j} = 0$ will not have a solution. To deal with it, should $a_{i,j} > \frac{1}{2}$ be found, $a_{i,j} = \frac{1}{2}$ is taken instead.

In Becke's population analysis scheme the last improvement is to replace the heaviside function and replace it with a more gradual type of "step-like" function. Hence a "cut-off" function is introduced and defined as follows [38]:

$$s_k(\mu_{i,j}) = \tfrac{1}{2}\left(1 - f_k(v_{i,j})\right) \tag{59}$$

Where if f_k chosen to be sufficiently steep, the heaviside function will be recovered. $f_k(v)$ is required to be odd for $v \in [-1, 1]$ and flat at the end points. To ensure these criteria are met a simple two term polynomial $p(v)$ is used. An iterative algorithm is then used to turn these functions into step function with increasingly sharp cut-off, with k being the order to which this algorithm is carried out.

$$\begin{aligned} &f_1(v_{i,j}) = p(v_{i,j}) \\ &f_2(v_{i,j}) = p[p(v_{i,j})] \\ &f_3(v_{i,j}) = p\{p[p(v_{i,j})]\}, \ldots \ \text{ where, } \ p(v_{i,j}) = \tfrac{3}{2}v_{i,j} + \tfrac{1}{2}v_{i,j}^3 \end{aligned}$$

With the new transitional function the total weight is expressed in a similar manner to eq (58) but now with a normalization factor to ensure proper weighting:

$$w_n^{(k)}(\mathbf{r}) = \frac{P_n^{(k)}(\mathbf{r})}{\sum_{m=1}^{N} P_m^{(k)}(\mathbf{r})} \ \text{ with } \ P_i^{(k)}(\mathbf{r}) = \prod_{j \neq i}^{N} s_k(\mu_{i,j}) \tag{60}$$

Using this more continuous cut-off over a heaviside function could be interpreted as moving from conventional rigid polyhedra to more fuzzy polyhedra. In Becke's paper it is shown that using this method for $k = 3$ [38], an accuracy is obtained that is similar to other partitioning methods available at the time, however the simplicity of this method made it very popular up until this day.

$$N_i = \int d^3 r n(\mathbf{r}) w_i(\mathbf{r}) \tag{61}$$

With the introduction of this section the need for a Becke type space partitioning was shown. This method is not only adopted in QNA-type xc-functionals [37, 39], another application is population analysis which partitions the space, to weight $n(\mathbf{r})$ for each atom resulting in an effective number of electrons present and attributable to a certain nucleus. For a nucleus labeled with i, the number of electron N_i is given in equation (61). In the NWChem user manual a recommendation is made to use Becke's partitioning for population analysis when diffuse functions are in the electron orbital basis set [15] hence for this thesis Becke's method was adopted.

2.2.6 Constrained DFT

Since the start of the DFT framework section the focus has been on unconstrained systems. For the application of DFT in this thesis: tin ion collisions with a hydrogen gas, we need to be able to define an ion. With section 2.2.5 on population analysis a methodology has been shown to find the (fractional) effective charge of a given atom. The question remains how to ensure that (at larger separations) the electrons are at the right place. The system needs to be constrained if we want a given amount of electrons to be bound to a specific nucleus. A constraint with N electrons on an nucleus c looks like this:

$$N_c = \sum_\sigma \int d^3r w_{c,\sigma}(\mathbf{r}) n(\mathbf{r}) \tag{62}$$

Where $w_{c,\sigma}$ is the weight associated to the population scheme used in your DFT calculations (such as the Becke population explained in section 2.2.5). With this constraint the solutions to the Kohn-Sham equations should and will be different compared to a normal free system (in cases of large separation). To minimize the energy under the constraint (62), we make use of a Lagrange multiplier.

In general terms, we are trying to find a maximum or minimum of function $f(x_1, x_2, \ldots, x_D)$ under the condition that $g(x_1, x_2, \ldots, x_D) = C$. Finding the point that satisfies both of the conditions simultaneously can be done by first writing [40]:

$$\mathcal{L} = f(x_1, x_2, \ldots, x_D) - \lambda(g(x_1, x_2, \ldots, x_D) - C) \tag{63}$$

Where λ is called the Lagrange multiplier. By then setting $\nabla\mathcal{L} = 0$ we obtain a system of equations which can be solved and results in:

$$x_1 = h_1(\lambda) \ \ , \ \ x_2 = \mathrm{H}_2(\lambda) \ \ , \ldots x_D = h_D(\lambda) \tag{64}$$

Substituting this back into the constraint $g[h_1, \mathrm{H}_2, \ldots, h_D](\lambda) = C$ then allows us to find λ, which in turn yields the exact maximum/minimum point under the constraint through eq (64) [40].

Now in the case of constrained DFT we recognize that we are dealing with a functional in our constraint:

$$N_c = \sum_\sigma \int d^3r w_{c,\sigma}(\mathbf{r}) n(\mathbf{r}) \equiv g[n](\mathbf{r}) \tag{65}$$

As we are trying to minimize the energy functional $E[n]$, we pick $f[n](\mathbf{r}) = E[n]$ and are left with:

$$\mathcal{L} \equiv W[n, V_c] = E[n] + V_c \left(\sum_\sigma \int d^3r w_{c,\sigma}(\mathbf{r}) n(\mathbf{r}) - N_c \right) \tag{66}$$

introducing Lagrange multiplier V_c. As in the general case we are after V_c. By demanding that $W[n, V_c]$ is at a stationary point $\left(\frac{\delta W[n,V_c]}{\delta n} = 0\right)$ it can be show that Kohn-Sham equations (31) transform into [41]:

$$\left[-\frac{1}{2}\nabla^2 + v_{s,\sigma}[n_\uparrow, n_\downarrow](\mathbf{r}) + V_c w_{c,\sigma}(\mathbf{r})\right] \phi_{i,\sigma}(\mathbf{r}) = E_{i,\sigma}\phi_{i,\sigma}(\mathbf{r}) \tag{67}$$

which nicely illustrates the importance of an appropriate choice of population analysis scheme. Note that the solution of orbitals is now very much dependent on the value of the Lagrange multiplier V_c. This means that for every iteration/ set of orbitals in the self consistent (SC) calculation, V_c needs to be found [41]. In order to proceed the whole DFT self consistent method needs to be changed. During a SC iteration, the previous / initial guess electron density is used to find the normal KS Hamiltonian. With an initial guess for V_c, eq(67) will be solved. With the new set of constrained orbitals we try to find a new better value of V_c. With the new V_c another new set of orbitals can be found and with that a new guess for V_c. This process will continue until the set of orbitals satisfy the constraint in eq (62). If the new orbitals satisfy the constraint in eq (62), this SC iteration of the ordinary DFT method is finished.

As to finding V_c, in the general example λ could be found through simple linear algebra, for V_c only numerical methods will work [41]. To find a minimum in $W[V_c]$ we can solve for the derivative $\frac{dW}{dV_c} = 0$, eq (68). Now crucially it can be shown that $W[V_c]$ is a strictly concave function, meaning that there is only one V_c corresponding to a minimum in $\frac{dW}{dV_c}$ [41]. Consequently searching for a solution to $\frac{dW}{dV_c} = 0$ can be carried out by using the gradient $\frac{d^2W}{dV_c^2}$ in an educated guess for the Lagrange multiplier used in the next CDFT iteration. $\frac{dW}{dV_c}$ and $\frac{d^2W}{dV_c^2}$ are given in (68) and (69) respectively.

$$\begin{aligned}\frac{dW}{dV_c} &= \sum_\sigma \sum_i^{N_\sigma} \left(\frac{\delta W}{\delta \phi^*_{i,\sigma}} \frac{\partial \phi^*_{i,\sigma}}{\partial V_c} + \frac{\delta W}{\delta \phi_{i,\sigma}} \frac{\partial \phi_{i,\sigma}}{\partial V_c}\right) + \frac{\partial W}{\partial V_c} \\ &= \sum_\sigma \int d^3r w_{c,\sigma}(\mathbf{r}) n(\mathbf{r}) - N_c\end{aligned} \tag{68}$$

and,

$$\frac{d^2W}{dV_c^2} = 2\sum_\sigma \sum_i^{N_\sigma} \sum_{a>N_\sigma} \frac{|\langle \phi_{i,\sigma}| \, w_{c,\sigma} \, |\phi_{a,\sigma}\rangle|^2}{E_{i,\sigma} - E_{a,\sigma}} \tag{69}$$

where the last sum over a runs over all the unoccupied orbitals $\phi_{a,\sigma}$ in the basis set [41].

2.2.7 Effective Core Potential

In the normal DFT a great deal has been put into solving the non-relativistic Schrodinger equation. However as it turns out, solving the relativistic Dirac equation (in an analytical way) is sometimes possible yielding more accurate results by including what is referred to as ”direct relativistic effects” into the calculation of electron wave functions [42]. In modern DFT a correction technique called an Effective Core Potential (ECP) is recommended to be included in DFT calculations with heavier atoms [30]. The ECP introduces some of these previously mentioned relativistic corrections to be used even in more complicated systems.

To understand what an ECP correction is and why they are important we write the explicitly the Dirac Hamiltonian $\hat{H}_D$ for an N electron system. [42, 43]

$$\hat{H}_D = \sum_i^N c\hat{\boldsymbol{\alpha}} \cdot \hat{\mathbf{p}}_i + (\hat{\boldsymbol{\beta}} - \mathbf{I}_4)c^2 + \hat{V}(\mathbf{r_i}) \tag{70}$$

where $\hat{p}_i$ is the momentum operator acting on the i-th electron. $\hat{\alpha}$ and $\hat{\beta}$ are given expressed using the Pauli matrices $\hat{\boldsymbol{\sigma}}$:

$$\hat{\boldsymbol{\alpha}} = \begin{pmatrix} \mathbf{0}_2 & \hat{\boldsymbol{\sigma}} \\ \hat{\boldsymbol{\sigma}} & \mathbf{0}_2 \end{pmatrix} \text{ and } \hat{\boldsymbol{\beta}} = \begin{pmatrix} \mathbf{I}_2 & \mathbf{0}_2 \\ \mathbf{0}_2 & -\mathbf{I}_2 \end{pmatrix} \tag{71}$$

With the Hamiltonian in eq (70) it is possible to obtain an analytical expression for the energy levels of an H-atom/ H-like ion with atomic number Z seen in eq (72). Here n is the principal quantum number and $\kappa = \mp(j + \frac{1}{2})$

$$E_{nk} = \pm c^2 \left[1 + \left(\frac{Z/c}{n - |\kappa| + \sqrt{\kappa^2 - (Z/c)^2}} \right)^2 \right]^{-1/2} - c^2 \tag{72}$$

By Taylor expanding eq (72) we find that the non-relativistic energy scales like $E \propto Z^2$ while the first order relativistic corrections goes like $E_{\text{rel-corr}} \propto Z^4$. Quasirelativistic Wood-Boring add citation? calculations on He,Ne,Ar,Kr,Xe and Rn show a similar $E_{\text{rel-corr}} \propto Z^{4.34}$ relation [42]. $E_{\text{rel-corr}}$ scaling like approximately Z^4 suggest that $E_{\text{rel-corr}}$ is more significant in heavier atoms which is the main reason why these corrections should be included for such cases.

The direct relativistic effects also causes the contraction of inner shell electron wavefunctions which results in a more effective screening of the nuclear charge [42, 43]. This in turn allows the outer shell wave functions to spatially extend outward further than without an ECP. These more indirect effects of a relativistic correction will play an important role when calculating the potential between atoms. Additionally the addition of corrective terms also impacts chemical bonds in the equilibrium length, vibrational constants, and binding energy.

As mentioned before the Dirac equation can only be solved analytically in highly favourable cases, however for DFT there is still some role for the relativistic orbitals in what is called the Frozen-Core Approximation [43]. Here the orbital calculation is split into two part, the inner shell orbitals and the outer "valence" orbitals. As the inner shell electrons are often not involved in chemical processes these are "frozen". The combination of a nucleus with a set of relativistic inner electron orbitals is referred to as a core. The normal Hamiltonian , including electron-electron interactions, is replaced by a a valence-only Hamiltonian which consists of normal electron-electron and nucleus potential terms for valence shells only, plus interaction terms between the core and electrons, and between two cores. In eq (73) we see an example of a valence only Hamiltonian for N_v valence electrons.

$$\hat{H}_v = \sum_i^{N_v} h_v(i) + \sum_j^{N_v} \sum_{i<j}^{N_v} g_v(i,j) + V_{cc} + V_{cpp} \tag{73}$$

V_{cc} and V_{cpp} refer to the core-core interaction potential and the core polarization potential [42] (both will be discussed shortly). h_v and g_v can be identified as as the single electron and double electron operator respectively and in ECP's are usually written in non-relativistic operator form:

$$h_v(i) = \tfrac{-1}{2}\nabla_i^2 + V_{cv}(i) \;\text{ and }\; g_v(i,j) = \frac{1}{|\mathbf{r_i} - \mathbf{r_j}|} \tag{74}$$

where more generally $\sum_j^{N_v}\sum_{i<j}^{N_v} g_v(i,j) \equiv \hat{W}$ as defined in equation (17). Here V_{cv} is the potential term for the interaction between a valence electron and all other cores. The assumption is that the core-valence electron potential is a superposition of atomic pseudopotentials leading with a Coulomb term [42]:

$$V_{cv}(i) = \sum_{\lambda}^{N'} \left(-\frac{Q_\lambda}{|\mathbf{r}_{\lambda/\mathbf{i}}|} + \Delta V_{cv}^{\lambda}(\mathbf{r}_{\lambda_\mathbf{i}}) \right) + \dots \tag{75}$$

Furthermore, like V_{cv}, the core-core term is presumed to comprise of a sum of atomic pseudopotentials:

$$V_{cc} = \sum_{\mu}^{N'} \sum_{\lambda<\mu}^{N'} \left(\frac{Q_\lambda Q_\mu}{|\mathbf{r}_{\lambda_\mu}|} + \Delta V_{cc}^{\lambda_\mu}(\mathbf{r}_{\lambda_\mu}) \right) + \dots \tag{76}$$

An ECP introduces the desired relativistic effects indirectly through parameterization of ΔV_{cv}^{λ} and $\Delta V_{cc}^{\lambda_\mu}$. There are two different philosophies on how this should be done, the Model Potential (MP) and Pseudo Potential (PP). Both parametrization methods need as input the core (inner shell) orbitals, meaning that most DFT ECPs have a basis set of orbitals per atom to efficiently construct V_{cv} and V_{cc}. The core polarization potential term V_{cpp} describes the potential arising due to the electric fields of a polarized core, where the level of polarization factor of such cores is evaluated at the Hartree Fock level of DFT [42, 43] which uses the multipole expansion for the electric fields. V_{cpp} has a cut-off function near the cores, because the multipole expansion tends to break down at small separations.

To conclude a DFT ECP replaces the first few inner electrons by cores and then treats the valence electrons separately. By parametrization of the potential terms between cores, and valence electrons and cores, relativistic effects can indirectly be added into the evaluation of the Schrodinger equation. By treating only valence electrons the DFT computations are sped up and in most cases show more accurate results. Both the quasirelativistic Wood-Boring calculations and analytic results from the Dirac equation indicate that relatvistic corrections scale by Z^4 meaning using an ECP is advised if heavier atoms are involved in a DFT calculation. Lastly ECPs are developed to be used with a given basis set, thus if one is to be incorporated this should be taken into account while searching for the right basis set.

2.3 Interpolation

With DFT, a function value of an interaction potential can be found for each point in space. For practical purposes such as dynamical simulations it would be required to evaluate this potential at many different positions in space whose coordinates will change depending on the initial conditions of the system. To speed up this process, the convention is to find a nice analytic function that describes the potential function sufficiently closely. Finding such a function can be difficult if not impossible if there is no general idea of what it would look like. Additionally having a interaction potential described by a higher dimensional function also complicates matters significantly. Subsequently the solution to this problem is to interpolate the function where the interpolant needs to be constructed efficiently by an algorithm to keep DFT calculations to a minimum. Interpolation methods are commonly used in the field of quantum-chemistry to describe potentials, an overview of possible techniques is given in [44]. From this review paper the decision was made to opt for the sparse grid method, whose algorithm will be explained now.

2.3.1 Sparse Grids

$$\phi_{l,j}(y) = \begin{cases} 1 - |y/h_l - j| & \text{if } y \in [(j-1)h_l, (j+1)h_l] \cap [-1,1], \\ 0 & \text{otherwise} \end{cases} \tag{77}$$

In a more general context the problem at hand is the efficient construction of approximations to multidimensional functions defined over some multidimensional domain. Methods trying to attain this feat tend to suffer from the curse of dimensionality, the exponentially increasing computational costs when considering additional dimensions. Sparse grid interpolation in particular tries to alleviate of this growth problem by constructing the interpolant out of a linear combination of tensors of one dimensional interpolation rules. Additionally the nodes (or function evaluation points) needed for the algorithm are nested[5].

To start we begin with defining a one dimensional interpolation rule for the domain $\Gamma = [-1, 1]$. For any 1-dimensional function f, a mapping can be defined for the domain Γ to polynomial space $\mathcal{P}$, see eq (78).

$$\begin{aligned} &\mathcal{U}^{m(l)} : \mathbb{C}^0(\Gamma) \to \mathcal{P}_{m(l)-1}\big([-1,1]\big) \quad \text{with,} \\ &\mathcal{P}_{m(l)-1}([-1,1]) = \text{span}\{y^\nu : 0 \leq \nu \leq m(l) - 1\} \end{aligned} \tag{78}$$

where $m(l)$ refers to the number of function evaluated points in order l or in mathematical terms, $Y_m = y_1, y_2, \ldots y_{m(l)} \in \Gamma$.

To uncover what $\mathcal{U}^{m(l)}$ could look like a basis set of functions is needed to form the interpolant. Suppose the goal is to create an interpolant for the function $f(y)$, given it is analytic f can be expressed in a sum of polynomials. In a similar way to vectors and wavefunctions, polynomials live in polynomial space $\mathcal{P}$ which means that there is a basis set of smaller polynomials that span a portion or all of the polynomial space. To span the space most efficiently the basis elements need to be orthogonal, hence for sparse grid interpolation sets of orthogonal polynomials are used. Examples of orthogonal polynomials include Hermite, Laguerre, Chebyshev, Legendre and Lagrange polynomials. For sparse grid interpolation Lagrange polynomials are customary and they are seen in eq (79).

$$\psi_j^l(y) = \prod_{i=1, i\neq j}^{m(l)} \frac{y - y_i}{y_j - y_i} \tag{79}$$

---

[5] Lower order nodes are used for higher order interpolation making it possible to reuse old function values.

here the y_i's represent the coordinates of points at which f is needed to be evaluated.

$$\mathcal{U}^{m(l)}[f](y) = \sum_{j=1}^{m(l)} f(y_j)\psi_j^l(y) \tag{80}$$

Since Y_m contains nested points a more convenient way to write the interpolant is through the surplus operator:

$$\Delta^{m(l)} = \mathcal{U}^{m(l)} - \mathcal{U}^{m(l-1)} \tag{81}$$

where now,

$$\mathcal{U}^{m(l)}[f](y) = \sum_{k=1}^{l} \Delta^{m(k)} \tag{82}$$

which concludes the description of the one dimensional interpolation rule. To generalize this scheme to a more general d-dimensions is surprisingly easy. First off, the domain and multidimensional lagrange polynomial are written as:

$$\Gamma_d = \bigotimes_{k=1}^{d} \Gamma \quad \text{and} \quad \Psi_{\mathbf{j}}^{\mathbf{i}} = \prod_{k=1}^{d} \psi_{j_k}^{i_k}$$

Additionally, it is always possible to rescale each dimension's domain individually and accordingly. By extension the same linear operations, the mapping $\mathcal{U}$ and surplus operator:

$$\Delta^{\mathbf{m(i)}} = \bigotimes_{k=1}^{d} \Delta^{m_k(i)} \ , \ \mathcal{U}^{\mathbf{m(i)}} = \bigotimes_{k=1}^{d} \mathcal{U}^{m_k(i)} \ , \ \mathcal{U}[f](\mathbf{y}) = \sum_{1 \leq \mathbf{j} \leq m(\mathbf{i})} f(\mathbf{y_j})\Psi_{\mathbf{j}}^{\mathbf{i}}(\mathbf{y})$$

Thus far the interpolant could have been constructed with any set of data points on the function. Yet the power of sparse interpolations lies in choosing only a sparse set of surplus operators $\Theta(L)$ effectively reducing the total required function sample size to a new set, $\Theta_m(L)$. The Sparse interpolant is depicted by $I_{\Theta(L)}$ and expressed below:

$$\begin{aligned} I_{\Theta(L)}[f](y) &= \sum_{i \in \Theta(L)} \Delta^{\mathbf{m(i)}} \\ &= \sum_{\mathbf{j} \in \Theta_m(L)} f(\mathbf{y_j}) \sum_{\mathbf{i} \in \Theta(L), \mathbf{m(i)} \leq \mathbf{j}} t_{\mathbf{i}} \Psi_{\mathbf{j}}^{\mathbf{i}}(\mathbf{y}) \end{aligned} \tag{83}$$

here t_i are a set of integer weights that are function dependent. The procedure needed to find these is beyond the scope of this master thesis but can be found in detail in [45]. The choice of sparse points (or sparse rule) is understandably quite influential on the out-coming interpolant function, thus the next section is devoted to explaining important considerations for which sparse rule to use.

2.3.2 Interpolation Errors

In principle any set of points $Y \in \Gamma_d$ can be used to find an interpolant for some arbitrary function. As an example a set of equally spaced points Y in $d = 1$ and $f(x)$ (eq (84)) are chosen. Normally one would expect the interpolant to describe $f(x)$ gradually better as l increases.

$$f(x) = \frac{1}{(1 + 12x^2)} \tag{84}$$

Yet for this particular circumstances (Lagrange interpolation, equally spaced points, and $\Gamma = [-1, 1]$) the interpolant will show an increasing error with respect to $f(x)$, especially near the domain borders. This effect is known as Runge's Phenomenon [46, 47] and is characterized by error ridden oscillatory behaviour near domain edges which get worse when increasing interpolation order. This last example used a very specific $f(x)$ but in principle any function that shows significantly steep peak like behaviour within Γ can suffer from Runge's phenomenon. The adoption of Chebyshev nodes (zeros of the chebyshev polynomials, see eq (85)) has been shown to return a decreasing interpolation error if l is increased, thus these type of nodes are widely used in Lagrange interpolation.

$$y_j = \cos\left(\frac{2j}{l}\pi\right), \quad j = 1, 2, \ldots, l \tag{85}$$

In interpolation, the Lebesgue constant typically denoted as λ gives an indication of the quality of the interpolant for a given set of nodes [45]. λ is found by taking the operator norm of the interpolant, $||\mathcal{U}^{m(l)}|| \leq \lambda_l$ where with a smaller λ_l usually a better interpolant is found[45]. Theoretically λ is linked to $m(l)$, where rapidly growing $m(l)$ tends to result in small λ_l and vice versa. For practical purposes a balance has to be chosen between limited node growth and a small Lebesgue constant. This is where sparse node selections rules come in as they use nested nodes and smart algorithms for node selection from the full set of Chebyshev nodes to find that optimal balance.

One of the more popular asnd well balanced selection rules is the Clenshaw-Curtis rule,

Clenshaw-Curtis:

$$\begin{gathered} y_1 = 0, \;\; y_2 = 1 \;\; , y_3 = -1, \\ \text{for } j > 3, \quad y_j = \cos(2^{-\lceil \log(j-1) \rceil}(2j-3)\pi) \end{gathered} \tag{86}$$

$$\text{with } \lceil x \rceil = \min\{i \in \mathbb{Z} : i \geq x\}, \text{ leading to } m(l) = 2^l + 1 \text{ and } \lambda_l = \tfrac{2}{\pi}\log(2^l) + 1$$

More types of selection rules and their advantages are covered in [45, 16]. The implementation of sparse in this thesis is done using the Tasmanian coding packages [16, 17] and will be discussed in more detail in section 3.1.2.

3 Methodology

In the development of GIonS V2 some simplifications and practical choices were made for the efficient and correct way to determine the semi-classical Sn^{q+} trajectories. In this section these will be introduced, put against theory, and justified.

3.1 Potential Energy Surface

A hydrogen molecule itself is not center symmetric, because of that neither will its potential energy function. The Coulomb and ZBL potential are center symmetric, meaning the function of the potential could be expressed with only one coordinate. An important step for a non-center symmetric potential is thus to find the dependence of the potential on all possible coordinates. The total energy will now thus be plotted against multiple coordinates, such a plot is dubbed a potential energy surface (PES). This section is devoted to explaining how a PES was constructed, describing the interaction energies of Sn^{q+} and $H_2^{(+)}$, starting with the way the interaction energy was found for a given distribution of nuclei.

3.1.1 DFT Code and Settings

In this thesis density functional theory formalism was adopted to evaluate the interaction energy between Sn^{q+} and $H_2^{(+)}$. Because of the easy availability and use of input files for automated computations, NWChem [15] has been chosen as the DFT-code. This section follows with a rundown of choices of xc-functional, DFT-basis and NWChem specific settings.

Owing to its influence even on standard DFT calculations, the first thing to consider is the exchange correlation functional. The most logical choice would be that of any rung 5 double hybrid functional like B2PLYP (which is supported in NWChem) yet the high computational costs are a limiting factor here. Instead the range separated hybrid functional rCAM-B3LYP was chosen. Where rCAM-B3LYP is similar to CAM-B3LYP but has a different composition of LDA and GGA functionals and has been found to have better performance for fractional systems of electrons [36]]. These kind of systems are to be expected due to the net charge on the tin ion, possibly causing a polarization within the molecular hydrogen. The full expression of rCAM-B3LYP is given in eq (87)[36].

$$\begin{aligned} E_{xc}^{\text{rCAM-B3LYP}} &= \alpha E_x^{\text{HF}} + (1-\alpha)E_x^{\text{Slater}} + \gamma \Delta E_x^{\text{B88}} \\ &+ \beta(E_x^{\text{LR,HF}} - E_x^{\text{LR,B88}}) + \delta E_c^{\text{LYP}} \end{aligned} \tag{87}$$

With $\alpha = 0.183$, $\beta = 0.94979$, $\gamma = 0.95238$, $\delta = 1$, and the range attenuation parameter $\mu = 0.33$.

For calculating a PES, DFT calculations will be done in bulk and with it some flexibility in basis set size, type of functions, and cardinal number is convenient to suppress computation times. Additionally the chosen basis set should also have access to an ECP and be available for the elements at hand. This is the reason the efficient Alrich (def2-XZVP) family of basis sets [48] has been used for this project. Not only does it meet the requirements just laid out, it also provides plethora of basis sets options with the possibility of adding polarization and diffuse function and doing so for a range of available cardinal numbers. In particular the basis set: def2-TZVPPD was used, where T indicates the cardinal number 3, P the addition of polarization functions, and D the inclusion of diffuse functions.

Furthermore the size and atomic number of Sn^{q+} warrants the use of an effective core potential. An effective core potentials needs to be matched to the used basis set. For def2-XZVP type basis sets the only available ECP is the Stuttgart-Cologne effective core potential [42].

The choice of NWChem as a DFT code, means that some NWChem specific choices also influence the results. For running NWChem, an input file is used. In the calculation of the data points for a PES, some settings are switched on or off if convergence cannot be met. An example is the use of symmetry, NWChem tries to automatically detect a symmetry and use it to speed up computations. Sometimes however this seems to break and abort the calculation. If the same input file is then used with auto symmetries off, the program will nicely converge. Additionally in any system where symmetries can or cannot be used, the program returns the same value up to fractions of eV's. Because of these observations symmetry will automatically be turned off and the input file run again if any abort of NWChem has been detected.

A similar problem exists with the use of either a spherical or Cartesian version of the same basis set. Here once again comparable results are found in cases where both converge. As with the use of symmetry, the input file starts out with a spherical basis set and switches to a Cartesian one if need be.

Currently the code is not able to distinguish between the different types of error (as it is managed by python and no error interpreter has been build yet). Consequently a hierarchy of changes has been implemented, where first the coordinate type of basis set is changed then auto symmetry will be turned off. If the problem hasn't been resolved yet the coordinate basis will be switched back and a combination of Cartesian and auto symmetry on will be tried. While this process sounds needlessly time consuming, the reality is that the DFT calculation usually aborts pretty quickly if either symmetry usage or the coordinate basis of the basis lay at fault.

Lastly, having small inter nuclear separations seems to lead to linear dependency problems of the basis sets. This should be resolved by NWChem automatically yet in some cases it does not seem to be able to handle it. From further inspection it looks like it is a CDFT specific problem as in all cases normal DFT (with q electrons removed but without constraint) does provide a total energy. From NWChem's CDFT documentation it is not clear what could be at cause, though the most likely explanation is that orbital orthogonalization is done differently (or not at all) in between steps when searching for the right Lagrange multiplier. For now this orthogonalization problem only seems to occur with H_2^+ if the Sn^{q+} is close by. By not using a constrained DFT but, DFT with $q + 1$ electrons removed we are essentially giving the electrons more freedom to arrange. Although it would be nicer to only use one or the other, using the normal DFT can be considered as an adequate approximation as at close separations electrons most likely have the freedom to arrange as they like anyways. If one of these instances does occur, the program has been designed to swap over to normal DFT, while issuing a warning that this has happened and with which inter nuclear coordinates.

One other way to get rid of these linear dependencies and obtain a result is by making the basis set smaller. Doing this is questionable at the very least as the difference between using a basis set with or without diffuse/ polarization functions could be significant. As such, a system that automatically reduces the basis set has been implemented but will raise a warning if it has been activated. The main reason why this system is still useful, is to find the edges of the domain of convergence of the initial basis set (with the other settings used).

For all the NWChem and DFT specific choices, a wide domain which allows for stable computation has been found. There are notable regions where linear dependencies seem to play a significant role. If the tin ion is placed close to the center of the hydrogen molecule, NWChem and the automated systems are not able to obtain a total system energy due to linear dependencies. The same seems to apply if the tin is placed in the region close to either of the hydrogen atoms. The approximate border of the stability domain will be shown in section 3.1.2 as it plays an important role in calculating the total potential energy surface.

3.1.2 Sparse Grids in PES Construction

Regardless of coordinate system, calculating an interaction energy using DFT comes at the cost of long computation times of about 5 minutes per data point needed. In this order of computational timescales the force and hence gradient are to be computed for each time step, which is very impractical as there is a need to redo simulations for every individual energy, impact parameter, and hydrogen orientation, see figure 4. In order to streamline the process the proposition is to use sparse interpolation. By constructing a sparse grid up to some order l over as big a domain as possible, the gradient can be determined with interpolated values. Ideally only one sparse grid is used that extends over the entire space. However as mentioned, the DFT application in NWChem has some convergence issues within regions of small inter-nuclear distances. The solution is to only interpolate a domain for the PES where these regions are excluded.

The question now is what kind of coordinate system is convenient? In GIonS the locations of particles are defined in ordinary 3D Cartesian coordinates. However for computational convenience and easier interpretation of the PES, a transform is made for a set of coordinates for Sn^{q+} and H_2 to a new frame with the center of mass of the molecular hydrogen at $\{0, 0, 0\}$. If the $H - H$ is chosen to be along a principal axis this operation reduces the description of the system to a new set of reduced coordinates $\{x'_0, x'_1, x'_2\}$. Finding a new convenient coordinate system and the transformation to it will allow for a general treatment of a Sn^{q+}, $\mathrm{H}_2^{(+)}$ collision regardless of initial orientation.

Molecular hydrogen is $O(2)$ symmetric which is characterized by a symmetry around the hydrogen bond axis. This is used to reduce the domain at which the PES needs to be evaluated to the plane which is spanned by the inter-nuclear vectors. A D_2 symmetry in this plane reduces the size of the domain even further to only a quarter of the total plane as seen in figure 9. Here ρ and z where chosen as axis labels of coordinate-system which is essential a cylindrical coordinate system. The PES domain is given by $\rho \in [0, \rho_{max}]$ and $z \in [0, z_{max}]$, where the domain edges should be chosen such that at these edges almost no potential energy is in the system. Within this square domain Tasmanian's sparse grid packages can be used to create a grid over this domain, which can be used for interpolation. Solely using a grid in these coordinates will lead to convergence problems as in the region $\rho \in [0, 0.3]$, $z \in [0, d + 0.15]$ linear dependencies tend to be a problem. We can circumnavigate this specific region by constructing two separate grids with domains $\rho \in [0.3, \rho_{max}]$, $z \in [0, d + 0.15]$ and $\rho \in [0, r_{max}]$, $z \in [d + 0.15, z_{max}]$. Near the H-nucleus a peak in PES is found which in both of these grids lays near the lower edge of the domain. Thus both of these interpolation grids will be prone to Runge's phenomenon as the peak-like behaviour is not confined to the center of either of these domains. Because of the need of a square domain other coordinate systems need to be considered such as a con-focal elliptical or toroidal system[6]. Both of these suggestions would allow for use of only one interpolation grid,

---

[6] For other coordinate systems an expression of the gradient isn't always readily available but can be calculated analytically using form factors.

however both also require computationally expensive and difficult inverse transformation. For that reason a more simple solution was considered for this thesis.

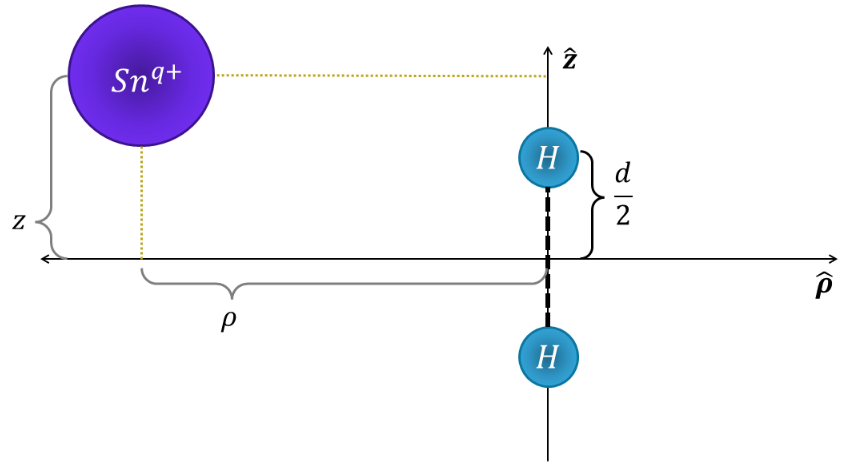

Figure 9: *Schematic showing the internal coordinates used for what is in this thesis referred to as the R-grid.*

Local to the hydrogen nucleus at $\{\rho, z\} = \{0, \frac{d}{2}\}$, the potential energy is likely somewhat symmetric in the semi-circle centered at the H and extending in the z-direction. Forming some sort of semi circle domain $r \in [0, r_{max}]$, $\theta \in [-\frac{\pi}{2}, \frac{\pi}{2}]$ around the H will then mean that each r_i approximately lays at one of the contour lines of the PES. If the PES is plotted for r, θ it result in something of sheet that increases with smaller r. Because of the need to calculate the potential energy with the tin ion as close as possible to the H_2, the PES coordinates don't center the circle at the hydrogen nucleus but at $\rho, z = \{0, \frac{d}{2} - r_{min} + 0.15\}$ to ensure a minimal separation to H of 0.15 a.u. along the axis of H_2, this is depicted in figure 10. With this semi circular domain there is still a need for an interpolation grid for $\rho \in [0.3, \rho_{max}]$, $z \in [0, d - r_{min} + 0.15]$. Luckily this can be attained by using a simple square grid in ρ, z coordinates. As this grid isn't particularly wide with respect to the relative peak height, the expectation is that the oscillations caused by Runge's phenomenon should be limited.

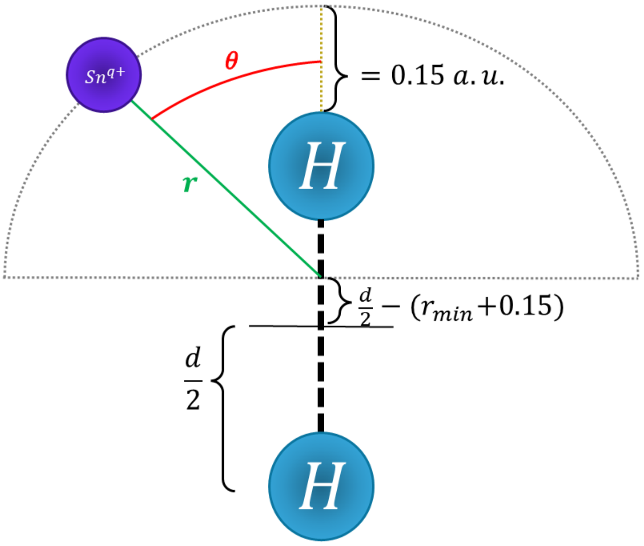

Figure 10: *Schematic showing the internal coordinates used for what is in this thesis referred to as the core-grid.*

Taking into account interpolation effects and DFT stabilities, a total set of data points needed to be calculated is shown in figure 11 where the circular grid has been transformed back into the more intuitive ρ, z system.

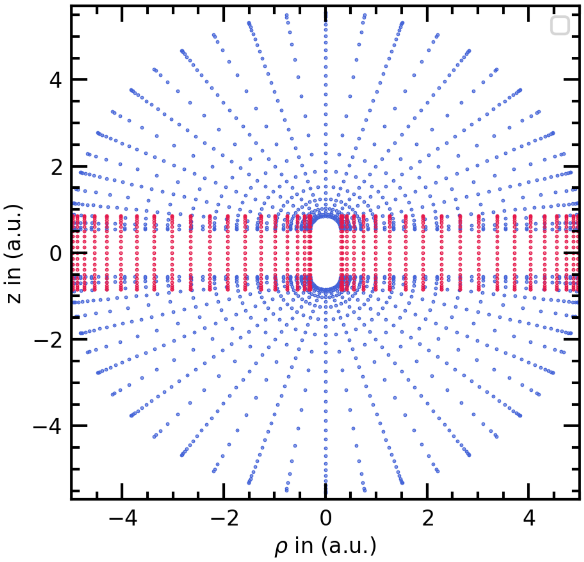

Figure 11: *Total set of Tasmanian sparse grid points used for interpolating the PES of the DFT potential. For the R-grid (red) an interpolation order $l = 20$ and Chebyshev rule were used. For the core-grid (blue) an interpolation order $l = 30$ and Clenshaw-Curtis rule were used. Note that this is the total set of points after mirroring along the z and rho axis.*

By now using the DFT settings and modules set out in the previous section the full PES has been constructed for this grid, in figure 12 you will see the PES interpolant for Sn^{1+} interacting with H$_2$ is shown[7].

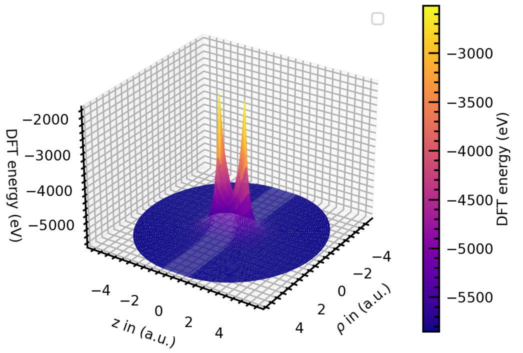

Figure 12: *PES of the interaction between Sn^{1+} and H$_2$. For the interpolation the grid points and setting shown earlier were adopted.*

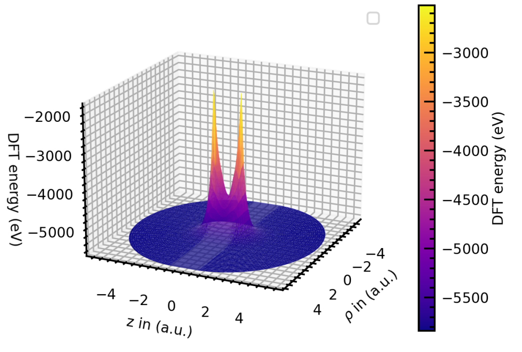

Figure 13: *PES of the interaction between Sn^{2+} and H$_2$. For the interpolation the grid points and setting shown earlier were adopted.*

3.1.3 Calculation of Gradient

With a calculated PES and a way to interpolate it, several types of finite difference methods can be utilized to determine the gradient of the potential at any point within the DFT domain. For this research three versions were considered, the forward difference, central difference to 1st order and central difference to 2nd order, they are all given in eq (88)[49]. All of these methods have been tested on the PES and in the end the 2nd-order central difference method was chosen. All three methods resulted in approximately the same magnitude of gradient in both the R and C-grid. But the use of interpolated data for the evaluation of a gradient might raise a few issues. The usage of Lagrange polynomials for fitting means some (small) residual oscillations might still be present within the PES regardless of interpolation depth l. This effect is reflected in the gradient which is more sensitive to them (i.e. any local minimum/maximum has $\frac{df}{dx} = 0$) in the worst case leading to nonphysical harmonic motion during a collision simulation.

$$\begin{aligned}
\left.\frac{df}{dx}\right|_{\mathrm{FD}} &= \frac{f(x+dx)-f(x)}{dx} + \mathcal{O}(dx) \\
\left.\frac{df}{dx}\right|_{\mathrm{CD,1st}} &= \frac{f(x+dx)-f(x-dx)}{2dx} + \mathcal{O}(dx^2) \\
\left.\frac{df}{dx}\right|_{\mathrm{CD,2nd}} &= \frac{-f(x+2dx)+f(x-2dx)+8f(x+dx)-8f(x-dx)}{12dx} + \mathcal{O}(dx^4)
\end{aligned} \tag{88}$$

With these finite difference methods the gradients of the PES were found, these are all show in appendix 7.1.

Within GIonS V2 discrete time steps dt are used for simulating the motion of the atoms.

---

[7] The data points found from all these calculations have been stored in a ".csv" file which can be loaded into GIonS V2 and subsequently automatically reconstruct the interpolant on start up using the c++ Tasmanian library ready to be used for dynamics simulations.

In combination with an oscillatory gradient, this could lead to a collision violating energy conservation if dt is not adjusted for properly. To explain the mechanism, imagine a tin ion traversing the potential of a near flat energy surface. The combination of a velocity v and a fixed time step dt will then correspond to calculating the gradient/force at fixed positions. For a totally flat PES nothing will happen, however if the surface looks like a sine wave, velocity/energy will possibly be gained at one time-step and lost at the other, this is schematically depicted in figure 14. If then these steps across the PES are too big, there is no guarantee the speed gains and losses will cancel out (which is what is desired for what is in essence a flat PES).

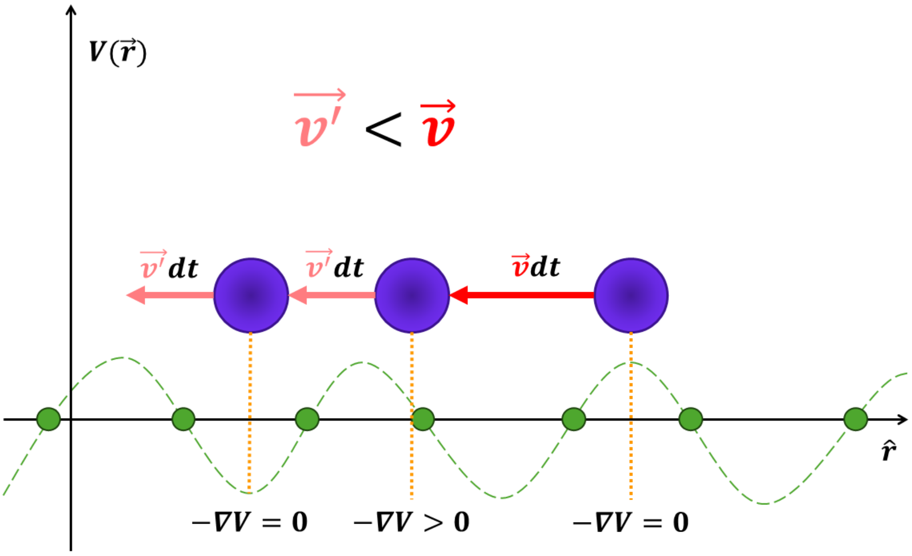

Figure 14: *A particle traversing a flat potential with some random oscillatory interpolation error. By traversing in discrete steps the atom gets slowed down losing energy, even though the data-points in lime green depicting the potential are completely flat.*

In order to rid the simulation of this energy breaking effect, dt is adjusted over time. In the ideal case fixed distance steps dx are taken that are significantly smaller than the wavelength of the oscillations. The time step at any moment t_0 in the simulation would then be given by solving:

$$dt(t_0) = \frac{dx}{|\mathbf{v}(t_0) + \mathbf{F}(t_0)dt(t_0)|} \tag{89}$$

However in GIonS V2 this seemed to be a unstable solution. The very next best thing was chosen instead, calculate $dt(t_0)$ without any force input, and scale it according to the ratio of the old and the new velocity:

$$dt(t_0) = \frac{|\mathbf{v}(t_0)|}{|\mathbf{v}(t_0) + \mathbf{F}(t_0)d\tilde{t}(t_0)|} d\tilde{t}(t_0) \quad \text{with} \quad d\tilde{t}(t_0) = \frac{dx}{|\mathbf{v}(t_0)|} \tag{90}$$

Additionally the time step isn't required to be small if the tin ion is significantly far away from the hydrogen atoms. Because of this dx is also varied based on the inter-nuclear separation. In order to retain the right size of dx (or dt) within the DFT grids a step function could be used. Here it was chosen to use the error function as it helps engineer in a smooth transition from one domain to the other. The function that scales dx, $f(\mathcal{R})$, is given in eq (91) and illustrated in figure 15.

$$f(\mathcal{R}) = 1 + \tfrac{\mathcal{R}}{20}[1 + \mathrm{erf}\,(\mathcal{R} - \mathcal{R}_{cut} - 2.3)] \quad \text{with} \;\; \mathcal{R} = \min\{|\mathbf{r}|, |\mathbf{r}_1|, |\mathbf{r}_2|\} \tag{91}$$

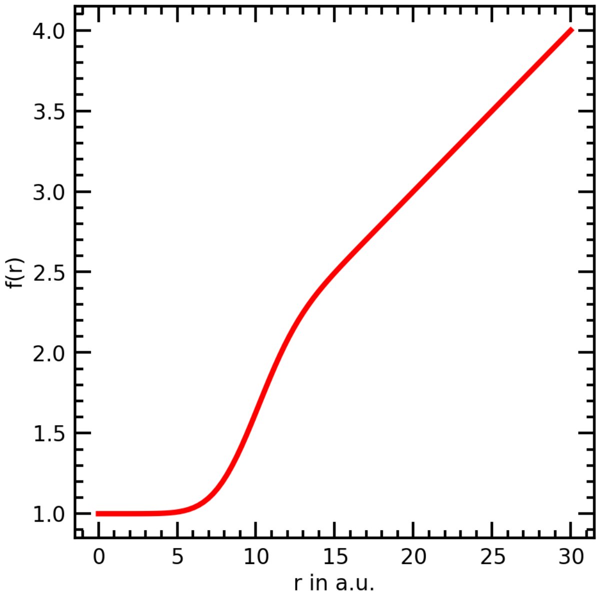

Figure 15: *$f(r)$-function engineered to increase the simulation step size dx as the inter-nuclear separation r increases. Here $\mathcal{R}_{cut} = 7$ a.u., see eq (91)*

Here $\mathbf{r}_1, \mathbf{r}_2, \mathbf{r}$ denote the distance from Sn^{q+} to hydrogen atom 1, to hydrogen atom 2, and to the center of the molecular hydrogen respectively. $\mathcal{R}_{cut}$ is chosen as the value of the upper domain of the DFT grid, which ensures that the transitional region starts just before entering the DFT grid. Now eq (90) is generalized to introduce the scaling:

$$dt(t_0) = \frac{|\mathbf{v}(t_0)|}{|\mathbf{v}(t_0) + \mathbf{F}(t_0)d\tilde{t}(t_0)|}d\tilde{t}(t_0) \quad \text{with} \quad d\tilde{t}(t_0) = \frac{dx}{|\mathbf{v}(t_0)|}f(\mathcal{R}(t_0)) \tag{92}$$

By comparing between simulation results of different dx it has been found that using a $dx = 0.005$ a.u. is sufficient to prevent any major energy discontinuities entering energy loss results.

3.1.4 Charge Distribution Surface

For each PES data point gathered the partial charge of each atom found with Becke's population partitioning method was also extracted. In order to use these partial charges effectively for the calculation of torque they need to be interpolated following from the same motivation as the PES. For this sparse grid interpolation was used once more. In the construction of the PES a lot of work went into finding the right grids and settings to keep oscillatory interpolation errors to a minimum. However the gradient of the charge surfaces is not of interest to us and thus less care has been put into optimizing their grids. Technically one could create a totally different set of grids for the partial charges but for convenience the choice was made to use the same grids and settings as the PES. The charge of one of the H_2-nuclei and Sn^{2+} are show in figure 16 and 17 respectively. For the other H-nucleus the same surface is used but mirrored in the $z = 0$ axis.

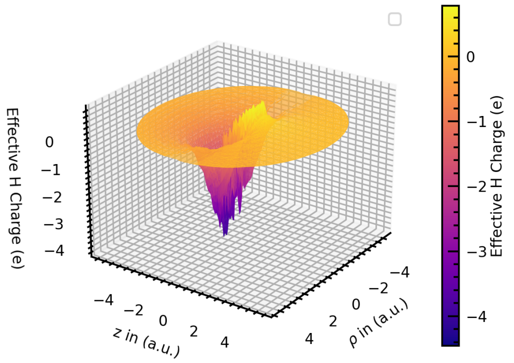

Figure 16: *Tasmanian sparse grid interpolant of the partial charge of a H-nucleus in the presence of a* Sn^{2+} *ion.*

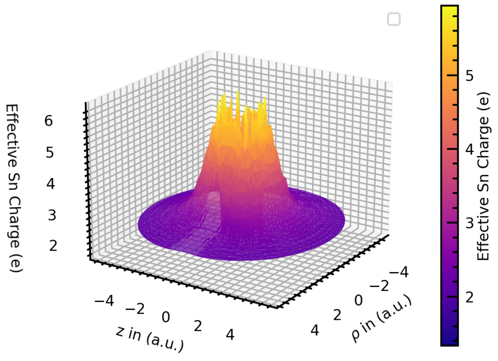

Figure 17: *Tasmanian sparse grid interpolant of the partial charge of a* Sn^{2+}*-ion in the presence of a H nucleus.*

In the first place it is immediately obvious that there is some oscillatory behaviour in the surface. This behaviour is caused by the interpolant function and not the DFT partial charges and this has been inferred by plotting the data points inside the same plot. These plots and interpolation grids are still useful despite the errors because the general trend along the surface is smooth and can thus be used for coupled torque calculations. Additionally, from further analysis of these surfaces it might also be possible to acquire some insight into the transition region between using DFT or CDFT or other DFT related quantities, though nothing apparent is visible here.

4 Results

The first thing investigated was the effect of rotational motion. By adding this motion to the simulations the influence of rotational dynamics has been probed. As the effective charge occupation of the nuclei has been found using DFT, a ZBL potential was used for this analysis (however GIonS V2 allows for the calculation of angular velocity even with other potentials such as the Coulomb or DFT-constructed potentials). To asses the relevance of these expanded dynamics the rotational energy put into the system has been calculated. The results for two initial energies $E = 0.1$ and $E = 10$ keV and some in plane orientations $\theta = \frac{\pi}{2}$, $\phi = 0, \frac{\pi}{2}$ are seen in figure 18. The energy put into rotation is seen to be very small and thus the induced rotational dynamics may be neglected.

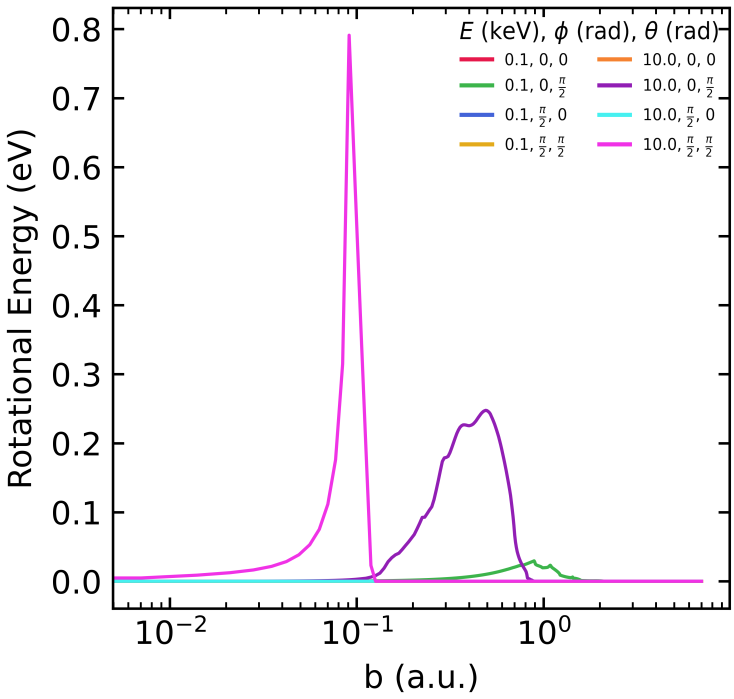

Figure 18: *Rotational energy gained versus impact parameter b during a collision of* Sn^{2+} *with* H_2 *using a ZBL potential.*

The reason why rotational motion is insignificant is related to the formation of coupled torque. For coupled torque to be applied to the H_2 one of the H-nuclei should have an effective charge above zero and the other below it. In any other configuration both forces will point approximately in the same direction (in the H_2 center of mass frame). Consequently angular velocity is only gained in the exclusive case that $\delta q_1 > 0$ and $\delta q_2 < 0$ or the other way around. By inspecting the surfaces depicting the partial charge of H in figure 16, we can see that this special case only occurs when the Sn^{q+} is almost on the bond-axis. Although tthe charge distribution is favourable, barely any torque will be generated because the components of the force perpendicular to the molecular axis will be small.

The combination of conditions needed to form a coupled torque prevents the system from picking up angular velocity in most initial conditions. It could be that a different description of these dynamics is necessary but for the rest of this project the decision has been made to exclude the rotational motion in further computations. This in part due to the computational cost of additional vector calculations.

4.1 Stopping Cross-Sections

For a representative stopping cross-section calculation, the determination of an appropriate maximum impact parameter b_{max} and density of impact parameter sample points, ρ_b is the first step to be taken. A combination of b_{max}, ρ_b is adequate if the power law coefficients in $S(E) = \alpha E^{\beta}$ describing the stopping cross-sections are not affected by the increase of either parameter. For calibration the known ZBL potential was chosen because the fitting results could be compared against the same fit found from SRIM data. Convergence is fast for b_{max} as is seen in figure 19. Thus the main concern lies with the impact parameter sampling, which seems to have converging fitting parameters to within 2 decimals at around $\rho_b \approx 50$. Similarly, with $\rho_b = 50$, α, β converge for $b_{max} \approx 5$ a.u. , to be certain of a good fit b_{max} was taken to be 40 a.u., twice the maximum value calculated in this convergence test. To be sure the b-settings $(b_{max}, \rho_b) = (40, 100)$ were adopted leading to the fitting parameters $\alpha = 0.52$ and $\beta = 0.49$ for a ZBL potential. In comparison, fitted SRIM data yields $\alpha = 0.89$ and $\beta = 0.48$. As β is more influential when comparing stopping lengths, the small difference between SRIM and GIonS V1 in β but not α seems reasonable. Hence a choice of $(b_{max}, \rho_b) = (40, 100)$ are appropriate settings for stopping-cross section integration calculations.

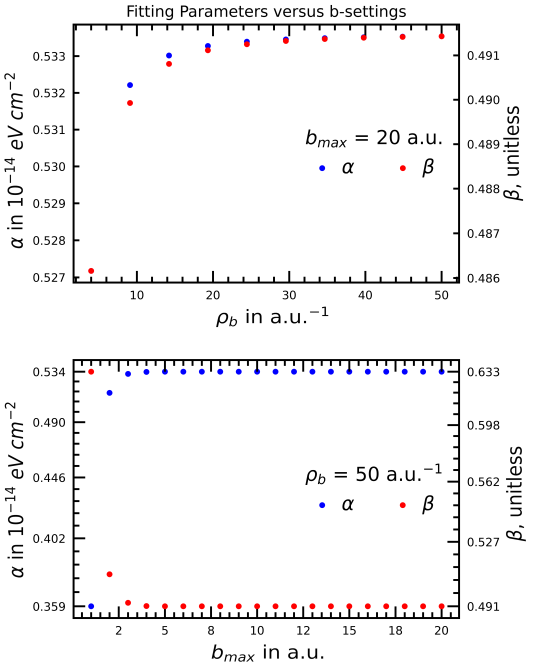

Figure 19: *Integration parameters b_{max} and ρ_b compared against the power law fit obtained from a ZBL potential.*

Next are some straightforward comparisons of energy loss per collision ΔE versus impact parameter b. To simplify matters we start by only looking at ground state $\mathrm{Sn}^{1,2+}$ collisions. Results of the GIonS V1 $\mathrm{Sn}^{1,2+}$ energy loss function ΔE are shown for several initial energies in figure 20. Because of the center symmetric ZBL used in GIonS V1, the orientation angles ϕ and θ don't actually matter. Interestingly there seems to be a shift in behaviour between small and large impact parameters which is dependent on the energy of the tin projectile. A logical argument exists that explains the change in energy loss behaviour by coupling the initial energy and impact parameter to the interaction time and with that energy transfer in the collision, this will be discussed later. This type of behaviour is not unique to the ZBL potential but can also be seen for a Coulomb type interaction potential as depicted in figure 21.

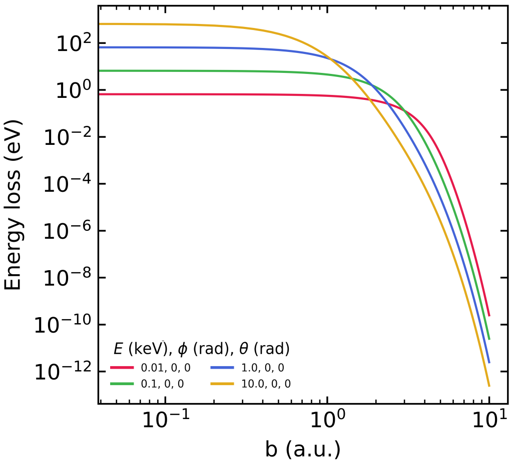

Figure 20: *Energy loss versus impact parameter for a* Sn^{1+} − H$_2$ *ZBL potential.*

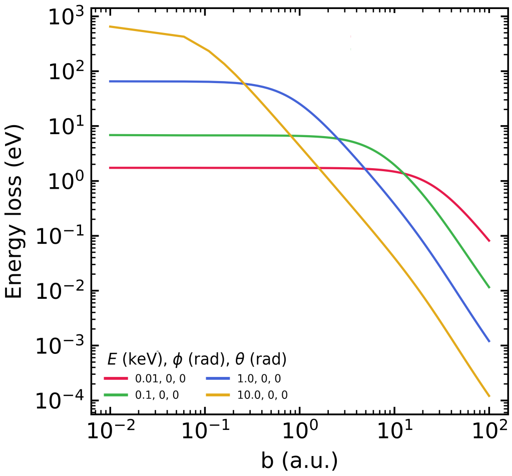

Figure 21: *Energy loss versus impact parameter for a* Sn^{1+} − H$_2^+$ *Coulomb potential.*

When inspecting the same results for a Sn^{1+} − H$_2$ DFT potential, figure 22, the overal trends are similar to the ZBL results, however oscillatory behaviour shows up in ΔE. This might be caused by small gradient oscillations that were not visible while checking the gradient of the PES. Depending on molecular orientation it might be possible to figure out if both or just one grid is "contaminated".

As depicted in figure 23,24 there is a noticeable difference in energy loss between the two extreme in-plane orientations with the DFT potential. However both orientations show similar noise features in approximately the same region $b > 2$. For a long time the hypothesis was that the fluctuations are rooted in the R-grid. For $\phi = 0$ the deflections and energy transfer would be impacted mostly by the gradient's ρ-component as that is now aligned with the y-axis. For $\phi = \frac{\pi}{2}$, the y-axis corresponds to the z component in the DFT frame thus being sensitive to the gradient's z-component. Regardless of orientation both of the two components of the PES gradient do influence the collision path. From just comparing two different orientation results it is thus not possible to figure out the origin of the oscillatory behaviour. Even so the argument that remains still claims that deflection away from/towards the hydrogen reduces/increases the interaction time considerably thus altering energy transfer.

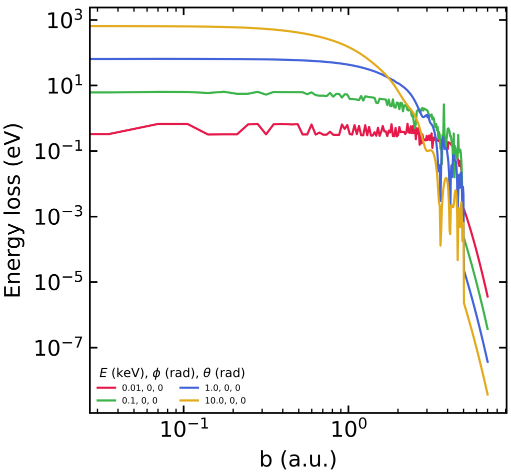

Figure 22: *Energy loss versus impact parameter for a* $Sn^{1+} - H_2$ *DFT potential with a molecule alignment of* $(\phi = 0, \theta = 0)$.

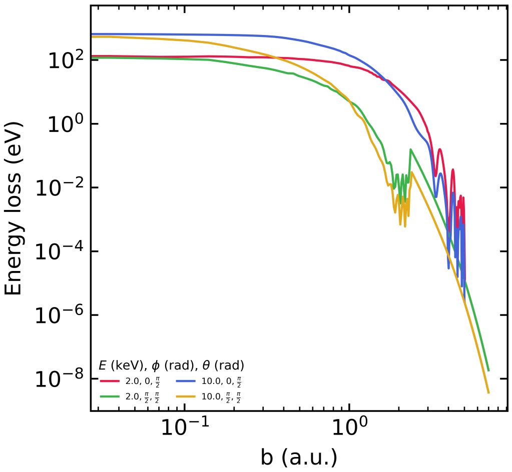

Figure 23: *Energy loss from a collision versus impact parameter for a* $Sn^{1+} - H_2$ *DFT potential, for two different molecule orientations* (ϕ, θ).

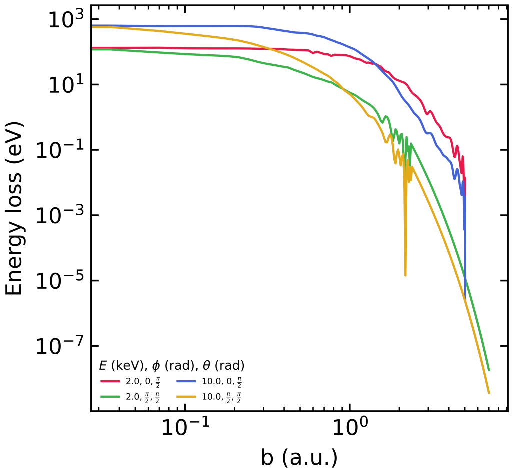

Figure 24: *Energy loss from a collision versus impact parameter for a* $Sn^{2+} - H_2$ *DFT potential, for two different molecule orientations* (ϕ, θ).

Another possible way to figure out the origin of the gradient oscillations is by increasing the interpolation order of a grid. This was done for the C-grid and R-grid which resulted in the oscillatory behaviour worsening drastically for the R-grid only, implying some sort of Runge's phenomenon still being at play. Yet the presence of oscillations can be by itself mitigating the error since an integral is taken over the domain of b and the amplitudes might cancel out. One note here is that ΔE is multiplied with the differential cross-section $2\pi bdb$ which makes error canceling less straight forward. In order to still use these results the choice was made to utilize the Savitzky Golay (SG) signal filter. This filter essential straightens out the energy loss data which should somewhat solve the problem and return a reliable energy loss spectrum if there is a nice harmonic type of noise. Stating that this last condition holds is reasonable for energies $E > 1$ keV. Below this limit ΔE contains so much noise it seems more like energy losses from some kind of chaotic collision/system. The explanation for this might be that at lower energy the relative size of the gradient oscillations and thus random energy losses are significant to the motion of the projectile. Just a small change in impact parameter could lead to a different path early on, which then cascades into a completely different trajectory at the bottom line. When looking at energies in the ranges $E \in [1, 10]$ keV, this type of chaotic results is no longer there, as seen in figure 22. Consequently, for the fitting of the stopping cross-section power law of a DFT potential only initial energies of $E \in [2, 10]$ keV were used initially as a conservative estimate. Another data set with energies $E \in [0.01, 2]$ keV was then added to the total set of stopping data points to create a second fit. The stopping cross-section as found by GIonS V2 are shown in figure 25.

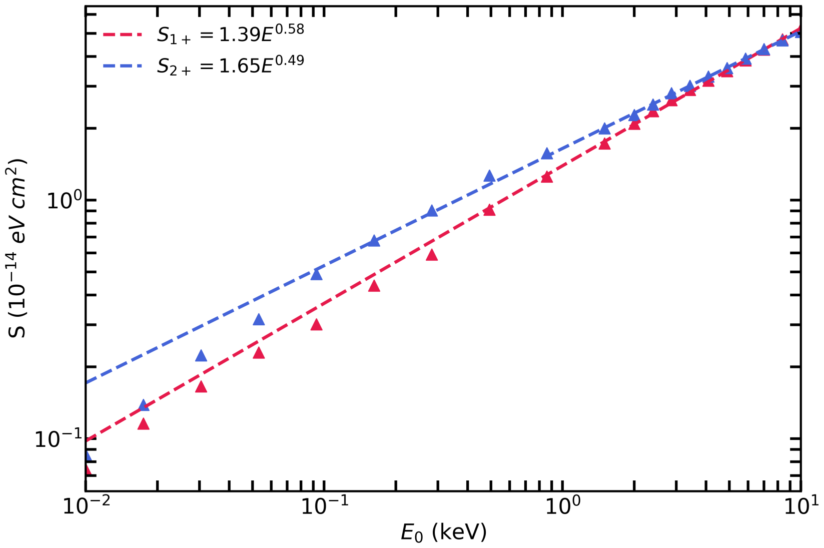

Figure 25: *$Sn^{1+,2+}$ with H_2 Stopping cross-sections for Sn^{1+} (red) and Sn^{2+} (blue) - H_2 collisions*

When looking at the two data sets of Sn^{1+} it seems that in the lower energy range, the model produces S_{1+}-values that are overal lower than predicted by both of the power law fits. This is partly due to the lack of knowledge on the uncertainty in S_{1+} which skews the fitting process to weight in the high value S_{1+} data points more. If a standard deviation of 5% is assumed in all the data points a fit of $S_{1+} = 1.34E^{0.61}$ is found which is close to the power law corresponding to only the lower energy stopping results. For both Sn^{1+} and Sn^{2+} stopping cross-section data has been published by Abramenko et al. [8] as previously mentioned. For comparison with these data sets GIonS V2's high energy regime results have been plotted in figure 26.

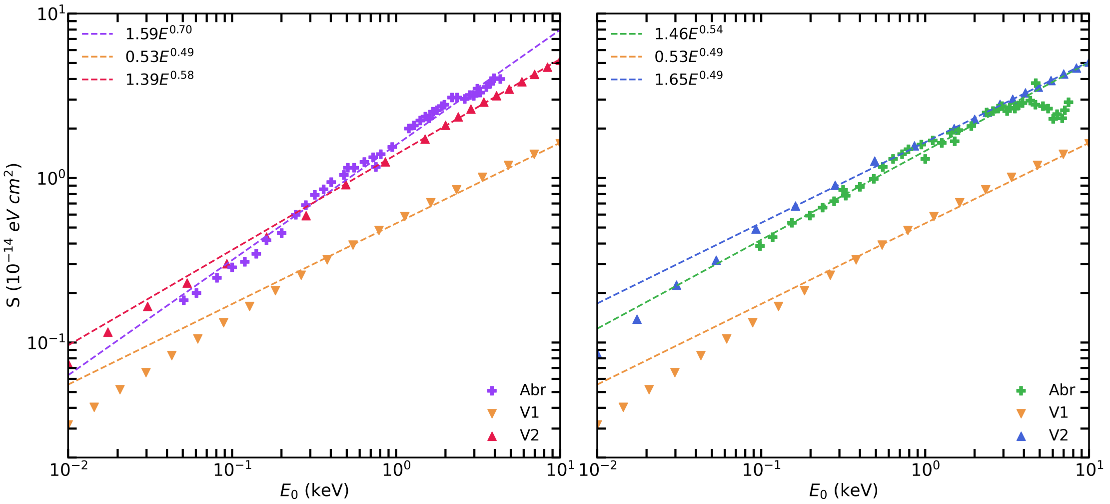

Figure 26: *Experimental stopping data from Abramenko et al.[8] and GIonS V1 & V2 predicted stopping,* S_{1+} *(left) and* S_{2+} *(right).*

In terms of the S_{1+} power law, a great step has been taken from GIonS V1 to V2, where $\alpha_{1+} = 0.53 \rightarrow 1.45$ is much closer to the Abramenko's data fit of $\alpha_{1+} = 1.59$. In terms of β_{1+} GIonS V2 also shows a promising improvement with $\beta_{1+} = 0.56$ being distinctly different from ZBL based models such as SRIM or V1 which have $\beta_{1+} \approx 0.5$. Additionally by allowing a fit to lower energy S_{1+} values $\beta_{1+} = 0.61$ would shift even further towards the $\beta_{1+} = 0.70$ measured by Abramenko et al.

For Sn^{2+} stopping, V2 also produces results in agreement with Abramenko et al. Once again the pre-factor of the stopping law is changed drastically between simulation versions moving closer to $\alpha_{2+} = 1.46$. No significant changes are found when it comes to β_{2+}, though with the new α_{2+}, the difference in $\beta_{2+} = 0.49, \beta_{2+} = 0.49$ could be more plausibly attributed to model or measurement error. More interesting however is that the dip in S_{2+} seen in Abramenko's S_{2+} from ~ 4 keV upward is not observed in the simulation results. Electron transfer of excited states of Sn^{2+} could have a different stopping cross-section which is an effect not taken into consideration in the V2 model and thus could be studied in the future.

One last interesting detail is the sudden increase in $S_{1,2+}$ seen around 0.3 keV for S_{1+} and 0.6 keV for S_{2+} in Abramenko data which now also shows up in GIonS's stopping cross-section data. For experimental results this could possibly be associated with measurement error or statistics but GIonS showing such behaviour could point at underlying physics included in GIonS, such as an interchange between two possible behavioral regimes in $S_{1,2+}(E)$. To investigate further the traces of the PES were taken near along different paths leading to one of the H-atoms, these traces are schematically shown in figure 27.

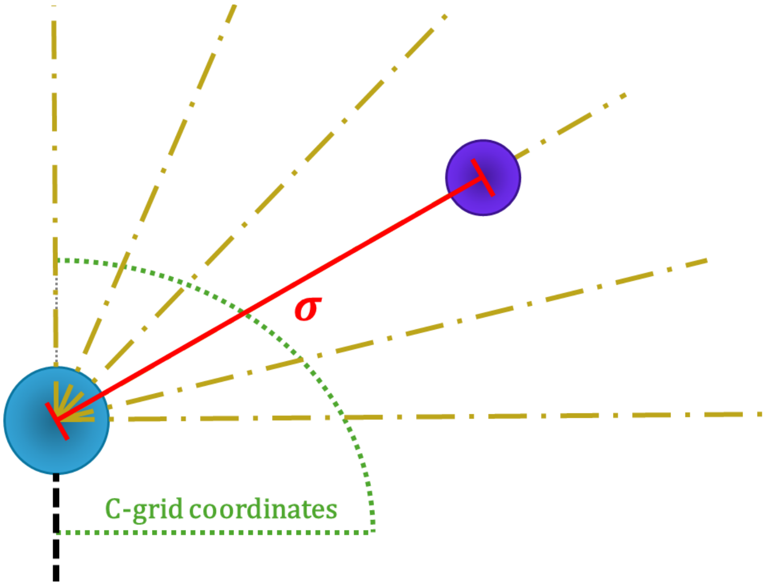

Figure 27: *Traces taken of the Sn*$^{1,2+}$ *PES. Note that the radial paths of the traces do not align nicely with the C-grid coordinate basis hence the introduction of the* σ *coordinate for further graphs.*

By now laying all the traces on top of one another figure 28 was created. Two things become apparent, one at the edges of the core grid there are still interpolation errors in the from of oscillations (though they are small). And more importantly the potential is (somewhat) symmetric in the semi circle around the hydrogen atoms in the H_2 as expected.

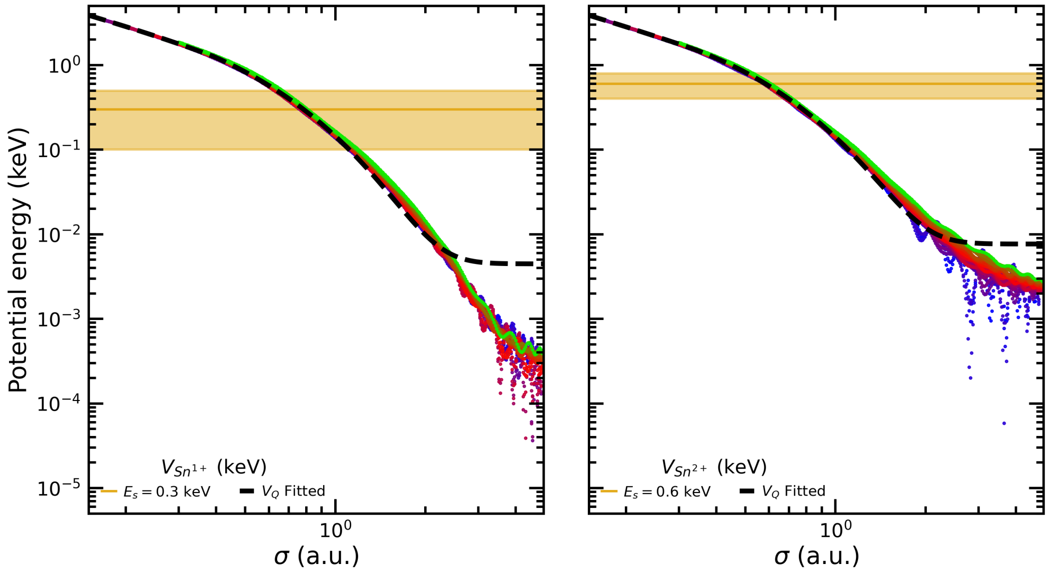

Figure 28: *All PES traces for the Sn^{1+} (left) and Sn^{2+} (right) DFT potentials layed on top of each other. The identified $S_{1,2+}$ transition energies have been plotted in at 0.3 ± 0.2 keV for S_{1+} and 0.6 ± 02 keV for S_{2+}*

When comparing the energies coupled to the supposed transition regions of $S_{1,2+}$ to the potential curves we see that they lay just before the potential switches behaviours from some power function $V \propto \sigma^{\gamma}$ to what appears to be an exponential relation $V \propto e^{\gamma' \sigma}$. Depending on the energy of the. If the $\sigma > 0.7$ really corresponds to a power law it is difficult to tell due to the range and interpolation error of the PES, but regardless the main point is that the PES behaviour changes.

To investigate the effect of a range separated potential a similar type of center symmetric analytic potential was made which shall henceforth be referred to as a quasi-DFT (QDFT) potential and is given in eq (93).

$$
\begin{gathered}
v_Q(\mathbf{r}) = \begin{cases} \left(\frac{a_0}{|\mathbf{r}|^{a_1}} - dv \right) & \text{if } |\mathbf{r}| \leq r_{cut} \\ \frac{a_2 e^{a_3 |\mathbf{r}|}}{|\mathbf{r}|^{a_4}} & \text{if } |\mathbf{r}| > r_{cut} \end{cases} \\
dv = \frac{a_0}{(r_{cut})^{a_1}} - \frac{a_2 e^{a_3 r_{cut}}}{r_{cut}^{a_4}}
\end{gathered}
\tag{93}
$$

The QDFT potential is fixed to have a transition point at r_{cut}. For $|\mathbf{r}| \leq r_{cut}$, v_Q behaves like a Coulomb potential (indicating nuclear repulsion) while at $|\mathbf{r}| > r_{cut}$ the potential is descibed by a screening like term (as seen in the ZBL-potential). By taking the gradient the interaction force is recovered, which is not continuous. To fix this in further analysis one could make use of some sort of smooth step function, but for now to keep it analytical the hard cut was chosen. We want to see stopping cross-sections that show different behaviour around some energy E_s which is now called the switch point. To see if this corresponds to the change in potential fit we need to control the energy barrier height of the QDFT potential at r_{cut}. The potential rescaling for a given split energy E_s is easily defined as:

$$V_Q(\mathbf{r}, E_s) = C(E_s) v_Q(\mathbf{r}) \\ \text{with,} \\ C(E_s) = E_s \cdot \left(\frac{a_0}{(r_{cut})^{a_1}} \right)^{-1} \tag{94}$$

For both the $q = 1+, 2+$ cases the QDFT potential was fitted and used as a center symmetric potential in the simulations. Additionally the same simulations were run again with the same potentials but divided by 3 and 6. By dividing V_Q, we are effectively lowering the energy of the switch point. Based off of the previous suspicions this will show a characteristic switch in stopping behaviour at increasingly lower energies. The QDFT stopping cross-sections are seen in figure 29

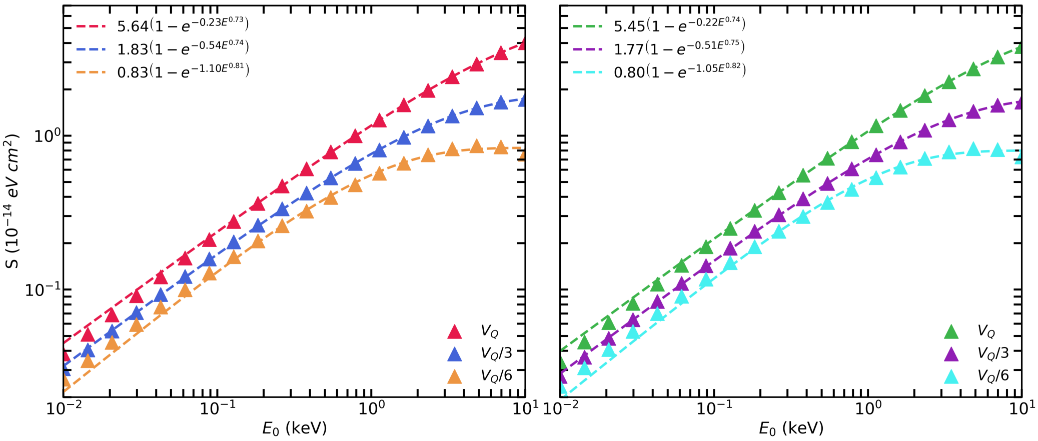

Figure 29: *Stopping cross-sections of the Sn^{1+} (left) and Sn^{2+} (right) QDFT potentials.*

In figure 29 the stopping cross-section data was not fitted to the conventional $S \propto E^\beta$ but rather $S \propto (1 - \exp\left[(-\gamma E^\beta)\right])$. This was done because of the exponential behaviour shown by the stopping cross-sections of these particular potential, though non power-law like behaviour is also seen in the ordinary DFT simulation results (fig 26). As the exponential relation seems to fit the data better it could indicate that at these energies we are entering the domain at which nuclear stopping (as seen in figure !!!!) starts to become less relevant[8]. Regardless, the curved data from the QDFT stopping results can be understood by looking at the stopping relations of the Coulomb potential, and V1 using a ZBL potential, depicted in figure 30.

---

[8] The same exponential fit has also been made on the V1 and DFT results and can be found in appendix B: sec 7.2

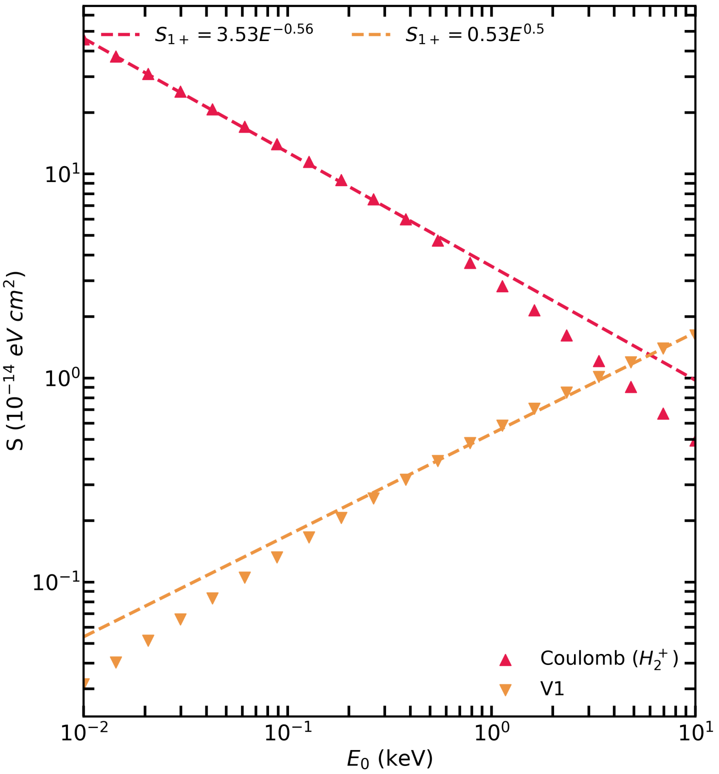

Figure 30: *Stopping cross-sections of a* Sn^{1+} *with* H_2^+ *Coulomb potential and the V1 model using the* Sn^{1+} *with* H_2 *ZBL potential.*

For the lower energies the stopping process consist mainly of a ZBL type stopping, while if the initial energy $E_0 \gg E_s$, the QDFT potential is dominated by the Coulomb term, thus giving Coulomb type stopping behaviour. This interchange thus leads to a morphing of the V1 into the Coulomb stopping curves. Now lowering E_s (like by dividing the potential by some factor) will make the transition happen at lower energies, this is completely reflected in figure 29. This last analysis has provided a very important result, every potential has its own characteristic stopping behaviour. If an interaction potential consists of several energy domains at which the potential has different behaviours, then this can be directly observed by a change in stopping behaviour at around the edges of these energy domains.

4.2 Further Energy loss Analysis

For this thesis the GIonS project has seen improvements in several departments most of which lean on the introduction of the Sn^{q+} and H_2 DFT interaction potential. In the end the main reason for modeling these interactions is to find the stopping cross-sections of tin with molecular hydrogen. Nevertheless from a theoretical perspective there is also some insight to be gained on the effect a certain interaction potential is expected to have on stopping power. By analyzing the relation between the energy-loss in a collision and the impact parameter b in particular. First to consider is energy-loss spectrum for different b and E, this has already been depicted in figure 20 and 21.

Here one can see that whether using a ZBL or DFT found potential, the energy loss spectrum of an initial energy $E_0 = E_i$ tin ion will always dip below an energy loss spectrum of lower initial energy $E_0 = E_j$ from some impact parameter $\tilde{b}_{i,j}$ onwards. For $b > \tilde{b}_{i,j}$ the energy loss spectrum is most likely dominated by the interaction time. Because higher initial energy collisions have less interaction time, they will have lower energy transfer during collisions at large impact parameters, which is reflected in all b versus ΔE plots (example, fig 20). Yet also for $b < \tilde{b}_{i,j}$ the energy loss is way higher for high energies. To further illustrate the effect of these two energy loss regimes lets define the partial stopping cross section:

$$\mathcal{S}(E_0, b_{min}, b_{max}) = \int_{b_{min}}^{b_{max}} \Delta E(E_0, b) 2\pi b db \tag{95}$$

By now using the transition impact parameter $\tilde{b}_{i,j}$, the total stopping cross-section can be partitioned:

$$S(E_0) = \mathcal{S}(E_0, b_{min}, \tilde{b}_{i,j}) + \mathcal{S}(E_0, \tilde{b}_{i,j}, b_{max}) \equiv \mathcal{S}_l(E_0) + \mathcal{S}_h(E_0) \tag{96}$$

Where as before $\tilde{b}_{i,j}$ indicates the impact parameter at which the energy loss spectra of energy E_i and E_j cross. Here by construction $\mathcal{S}_l(E_0) > \mathcal{S}_l(E_0')$ and $\mathcal{S}_h(E_0) < \mathcal{S}_h(E_0')$ for $E_0 > E_0'$. For the total stopping cross section $\mathcal{S}_l$ is the dominant term as higher energy tin ions experience more stopping but, what is not clearly visible here is the contribution of $\mathcal{S}_h$. Depending on the value of $\tilde{b}_{i,j}$ the contribution of $\mathcal{S}_h$ might or might not be significant for the total stopping cross-section. This is especially true because of the differential cross-section $2\pi b$ term, see eq (95). If $\tilde{b}_{i,j}$ decreases, so will the difference in stopping cross section at energies E_i and E_j. Having $\tilde{b}_{i,j}$ be affected over a whole range of energies will decrease the factor β in the power law describing the stopping cross-sections. Now the most important realization comes in the idea that $\tilde{b}_{i,j}$ could be interpreted as a range of interaction associated with the potential used in the stopping simulation. A comparison between the ZBL potential $V_{\mathrm{ZBL}} \propto \frac{1}{r} e^{-\gamma r}$ and Coulomb potential $V_{\mathrm{C}} \propto \frac{1}{r}$ is easily made as an example to support this hypothesis. In figures 20, 21 the energy losses for both the ZBL and Coulomb potential are shown where for the energies of 1 and 10 keV, $\tilde{b}_{\mathrm{ZBL}} \approx 1$ a.u. and $\tilde{b}_{\mathrm{Coul}} \approx 0.3$ a.u. . These then correspond to β fits of $\beta_{\mathrm{ZBL}} = 0.49$ and $\beta_{\mathrm{Coul}} = -0.42$[9]. This does not match up with the initial hypothesis on the physical interpretation of $\tilde{b}$ as the ZBL potential is meant as a screened version of the Coulomb potential meaning the Coulomb potential would always have a longer interaction range and thus $\tilde{b}$. Here $\tilde{b}$ itself does not seem to correspond to interaction range, rather at high enough energies the *Sn* gets closer to the nucleus, here the force of the ZBL is way larger. By looking at the crossing between the 0.1 and 0.01 keV curves we find $\tilde{b}_{\mathrm{ZBL}} \approx 3$ and $\tilde{b}_{\mathrm{C}} \approx 14$. This implies that the points of these crossings are not only range dependent but also dependent on the gradient of the potential.

---

[9] For the Coulomb potential a higher $b_{\max}$ needs to be used for a good fit because the losses don't drop fast enough as seen in figure 21

Because the ZBL and Coulomb potentials have very different gradients it is difficult to compare them based on $\tilde{b}$ alone. But the DFT potentials do have a similar gradient because of the outer extend of the potential is formed by electron-electron interactions which were calculated with the same xc-functional which is engineered to behave like $v_{xc}(\mathbf{r}) \propto -1/|\mathbf{r}|$ for individual electrons, see 2.2.4.

Because the DFT potentials for H_2 are not center symmetric they also serve as a great tool to test the $\tilde{b}$ hypothesis. A difference in stopping is found by comparing the two in plane ($\theta = \frac{\pi}{2}$) orientations with $\phi = 0, \frac{\pi}{2}$. With $\phi = \frac{\pi}{2}$ the stopping is greater because the $H - H$ bond extends into the direction of b meaning it's potentials is more prevalent at increased impact parameter, though at $\phi = 0$ generally the interaction time during a collision is larger.

By inspecting the energy loss spectra in figure 23 and 24, a similar conclusion can be drawn as before for Sn^{1+}, where here for the energies of 2 and 10 keV, $\tilde{b}_{\phi=0} \approx 1$ and $\tilde{b}_{\phi=\pi/2} \approx 1.8$. Subsequently from these energy loss spectra the stopping power law fit can be carried out. Paying attention to the $b < \tilde{b}$ regime, $\Delta E_{\phi=0} > \Delta E_{\phi=\pi/2}$ which is most likely an effect caused by the longer interaction times for $\phi = 0$.

The importance of interaction range is also reflected when comparing the DFT potentials of Sn^{1+} and Sn^{2+} with one another. During the DFT calculations electron-electron energies are also present in the total potential energy, implying their spatial distribution matters. The interaction of tin electrons with hydrogen electrons will extend the interaction range of the potential as the electron orbitals extend far from the nucleus in the case of nuclei with a high proton number Z such as Sn. If the fundamental difference between ZBL and DFT like potentials is the extend of the electron orbitals, there should also be a significant difference in power law between Sn^{1+} and Sn^{2+}. Sn^{2+} is optically smaller than Sn^{1+} as with the removal of an electron off Sn^{1+} the electron wave functions spatial extend diminishes. Fortunately for the hypothesis a difference in stopping between Sn^{1+} and Sn^{2+} is exactly what has been found in the previous section. Looking at figure 31 and 32, once again the energy transfer distribution is depicted for 2 and 10 keV ions where here $\tilde{b}_{1+} \approx 1.9$ and $\tilde{b}_{2+} \approx 1.6$.

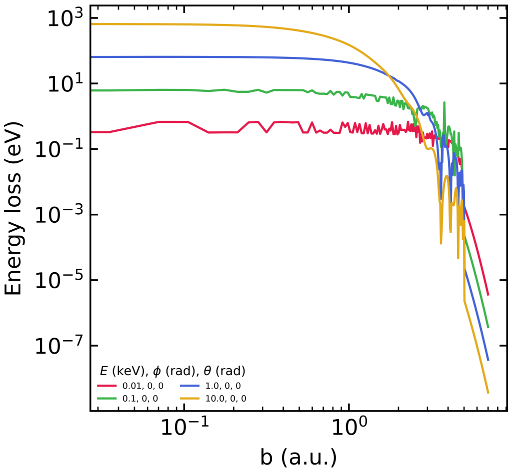

Figure 31: *Energy loss from a collision versus impact parameter for a* $Sn^{1+} - H_2$ *DFT potential, one orientation.*

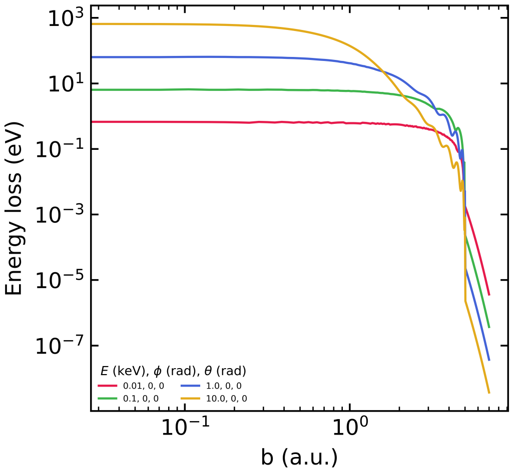

Figure 32: *Energy loss from a collision versus impact parameter for a* $Sn^{2+} - H_2$ *DFT potential, one orientation.*

The impact electron orbitals seem to have on the power law also implies a possible relevance of excited states of both projectile and target. In order to show this one could calculate the exact stopping of an excited state tin ion with DFT. However at the moment of writing this thesis, an excited state potential can only be created by shifting the ground state potential energy up leaving the gradient invariant. With that any excited channel with or without electron transfer would yield the same stopping cross-section as the ground state (assuming electron transfer is possible in both states). Calculating excited state energies is very much possible within the framework of DFT by making use of linear response theory [23]. This theory falls under a branch of DFT called Time Dependent Density Functional Theory or TDDFT in short [24]. With linear response theory, the first n excited state energies can be computed. The use of TDDFT and linear response theory was considered during this research, during which TDDFT was able to recover the first few energy levels of Sn^{2+} and H_2^+ to within fractions of eV's but only independently. In a combined system and at large separation the first many excited states of that system would correspond to excited states of molecular hydrogen. In particular TDDFT would find Sn^{2+} excited states only after all hydrogen's excited states with energy difference lower than the first excited state of Sn^{2+} at 6.64 eV were found. This in itself is not problematic but would require extensive calculations. Nevertheless whenever internuclear distances are small it is not clear which level corresponds to what was initially an excited tin ion at large separations. This problem is most likely universal to the calculation of any type of DFT potential and thus needs to be solved in order to make actual excited state interaction potentials. A solution could be to save the orbital vectors of excited Sn^{2+} without any H_2 present and then use these vectors as a starting point when doing an ordinary DFT calculation with H_2 added back in. NWChem possesses the capability to try this procedure, but as of yet it hasn't been tested over a wide domain.

The entire argument in the last few paragraphs supports a conclusion that the power law is significantly influenced by the range l and gradient of the interaction potential. On top of that l is likely related to the number of interacting electrons and it is also conceivable that the quantum states these electrons are in play a role. Excited state ions may have higher stopping power then if they were in the ground state. Reflecting these thoughts on the stopping of tin ions, it follows that the prediction is that higher charge states have smaller stopping cross-sections. Yet if their electron transfer cross-sections are sizeable even highly charged ions will still be stopped, though electron transfer will play a bigger role in making an accurate total stopping length predictions.

5 Conclusion

The GIonS V2 model introduces the possibility of using new tailor made potentials for the interaction between ions and matter. With it new numerical techniques, mathematical descriptions and physics was brought together into a final result. This final result shows that ground state DFT potentials are an excellent choice to descibe the dynamics that are at play during low energy tin ion stopping as simulation results show good resemblance to experimental data. Most importantly, the newest version of GIonS does not indicate the significant drop in Sn^{2+} stopping cross-sections from about 3 keV and upward found in Abramenko's results as real.

Some additional analysis has pointed at the idea that each potential has its own stopping behaviour. Furthermore any potential that is energy range separated into two or more potential behaviours, will see a interchange from one to the other corresponding stopping function close to the energy at which the potential switches behaviour. This is most relevant for most types of nuclear stopping as at high energies one would expect a Coulomb type potential while at lower energies the interaction is mediated by some type of screened Coulomb term.

In the DFT potentials these two regimes are easily identified and can be arguably be traced back to the choice of Core Potential taken. Here the Coulomb type interaction is most likely related to the core-core term and the screened Coulomb to the core-valence term. Following this argumentation it could be possible to fit core potential parameters based of off stopping data.

The results of the GIonS model show great promise especially as there is still a lot of potential left untapped. Some of the possible improvements are now listed.

The first big upgrade GIonS could receive is a more dynamical treatment of the molecular $H - H$ bond, which was chosen to be rigid. By doing so no vibrational motion was modeled into the collision. Vibrations within the H_2-molecule could significantly impact the possibility of the H_2 to pass an electron to the Sn^{q+} because potential curve crossing moves as the hydrogen atoms move apart. Additionally if electron capture does occur, the H_2 bond will shrink in size to its new H_2^+ equivalent equilibrium bond length ($1.4 \rightarrow 2.0$ a.u), the process and way in which this happens is not known and also not modelled in any way in GIonS yet. Consequently the model's performance on loss-channels with electron transfer could be improved by treating these problems which would start at making a PES with the bond length d as another (internal) coordinate (something which has been prepared but not worked out yet). Lastly the presence of a tin ion near a H_2 could induce some sort of bond relaxation, though the short interaction time might prevent this from happening. Even so assuming it is a possibility the new bond length could be calculated by optimizing the energy over the internal the bond length. Doing so might alter the PES in such a way that the stopping results turn out differently. This optimization has not been implemented in GIonS V2 because as mentioned prior NWChem does not provide the option to optimize over internal coordinates.

When it comes to technical elements there are two areas of improvement. Firstly the process of interpolation could more streamlined. With the use of sparse grids the necessary task of interpolating the PES was made possible though only after finding an optimal set of grids and settings under which no huge interpolation errors were evident. For sake of simplicity it would be good if the model could reduce the number of grids from two (R and core grid) to one. This could be facilitated by using a different coordinate system around H_2 such as elliptical coordinates. Another possible way to do so is by using a different interpolation method all together. If looking for a pre-written library the advise would be to ensure it is supported in both Pyhton and c++ merely for convenience. Otherwise big parts of GIonS V2 might need to be rewritten. Secondly because of computational times it might also be worth the effort to prepare GIonS to run on a cluster. Because I have no personal experience with this I have no way of telling what level of difficulty this task entails but it would allow for more time to debug the code if it ends up working.

There are also ways the DFT part of the code could be improved. The xc-functional used is a hybrid and thus of fourth-rung but fifth rung functionals also exist and it would be interesting to see whatever the difference is between the two in these type of calculations. Furthermore by adopting time-dependent DFT or TDDFT in short, the PES of excited states of ions might also be constructed and used to further study the effect of electronic configuration on stopping cross-section. More details on possible methods to use TDDFT are in the previous section.

Lastly, possibly the best upgrade GIonS could receive is a successful construction of a $\mathrm{Sn}^{(q-1)+}$ and H_2^+ potential as it would allow for electron transfer channels to be included into the model. By shifting the ground state PES up according to the NIST excited state energy levels [50] the model would be able to allow for electron transfer to occur by using the same Landau-Zener model calculation as done in GIonS V1 but now with a more accurate crossing radius. This opens op a lot of possibility as V2 will already automatically calculate the electron transfer probability and thus cross-sections of the collisions. Furthermore it was also anticipated that V2 might have been able to do a two level multi level Landau-Zener calculation by using a PES of excited state energies but it was not possible due to the lack of $\mathrm{Sn}^{(q-1)+}$ and H_2^+ potential data.

6 Acknowledgment

In the process of writing this thesis I had plenty of discussions and feedback from a plethora of people from both the QISD group and ARCNL's Source Department. First off a special mention to my first and second examiners, Prof. Dr. Ir. Ronnie Hoekstra and Dr. John Sheil. Their constructive criticism and perspectives have lead me to crucial insights which culminated in a well informed and extensive analysis of the project's results. Almost equally important is the help of Dr. Emilia Olsson whose guidance into the world of DFT has enabled me to develop the code and underlying physical description to its current form. Additionally I would like to thank all the PhD's in the QISD group (Emiel de Wit, Klaas Bijlsma and Luc Assink) for their support in regards to short discussion on intermediate results and their advise on how to clearly communicate these during update meetings and presentations. The last special thanks I want to attribute to the master students Lennart Tinge and Fleur Veen. Working from the same office for about a year has been thought me more about high voltage experimental setups and water droplets than I will ever need to know, but most of all, it was always very fun to come to campus because of these two.

References

[1] G.E. Moore. Cramming more components onto integrated circuits. *Proceedings of the IEEE*, 86(1):82–85, 1998. doi: 10.1109/JPROC.1998.658762.

[2] Gordon E. Moore. Progress in digital integrated electronics [technical literaiture, copyright 1975 ieee. reprinted, with permission. technical digest. international electron devices meeting, ieee, 1975, pp. 11-13.]. *IEEE Solid-State Circuits Society Newsletter*, 11(3):36–37, 2006. doi: 10.1109/N-SSC.2006.4804410.

[3] Oscar O Versolato. Physics of laser-driven tin plasma sources of euv radiation for nanolithography. *Plasma Sources Science and Technology*, 28(8):083001, aug 2019. doi: 10.1088/1361-6595/ab3302. URL `https://dx.doi.org/10.1088/1361-6595/ab3302`.

[4] O O Versolato, J Sheil, S Witte, W Ubachs, and R Hoekstra. Microdroplet-tin plasma sources of euv radiation driven by solid-state-lasers (topical review). *Journal of Optics*, 24(5):054014, apr 2022. doi: 10.1088/2040-8986/ac5a7e. URL `https://dx.doi.org/10.1088/2040-8986/ac5a7e`.

[5] F. Torretti, J. Sheil, R. Schupp, M. M. Basko, M. Bayraktar, R. A. Meijer, S. Witte, W. Ubachs, R. Hoekstra, O. O. Versolato, A. J. Neukirch, and J. Colgan. Prominent radiative contributions from multiply-excited states in laser-produced tin plasma for nanolithography. *Nature Communications*, 11(1):2334, May 2020. ISSN 2041-1723. doi: 10.1038/s41467-020-15678-y. URL `https://doi.org/10.1038/s41467-020-15678-y`.

[6] Sasa Bajt, Jennifer B. Alameda, Troy W. Barbee Jr., W. Miles Clift, James A. Folta, Benjamin B Kaufmann, and Eberhard Adolf Spiller. Improved reflectance and stability of Mo/Si multilayers. *Optical Engineering*, 41(8):1797 – 1804, 2002. doi: 10.1117/1.1489426. URL `https://doi.org/10.1117/1.1489426`.

[7] Qiushi Huang, Viacheslav Medvedev, Robbert van de Kruijs, Andrey Yakshin, Eric Louis, and Fred Bijkerk. Spectral tailoring of nanoscale EUV and soft x-ray multilayer optics. *Applied Physics Reviews*, 4(1):011104, 03 2017. ISSN 1931-9401. doi: 10.1063/1.4978290. URL `https://doi.org/10.1063/1.4978290`.

[8] D. B. Abramenko, M. V. Spiridonov, P. V. Krainov, V. M. Krivtsun, D. I. Astakhov, V. V. Medvedev, M. van Kampen, D. Smeets, and K. N. Koshelev. Measurements of hydrogen gas stopping efficiency for tin ions from laser-produced plasma. *Applied Physics Letters*, 112(16):164102, 04 2018. ISSN 0003-6951. doi: 10.1063/1.5025914. URL `https://doi.org/10.1063/1.5025914`.

[9] S. S. Harilal, Beau O'Shay, and Mark S. Tillack. Debris mitigation in a laser-produced tin plume using a magnetic field. *Journal of Applied Physics*, 98(3):036102, 08 2005. ISSN 0021-8979. doi: 10.1063/1.1999851. URL `https://doi.org/10.1063/1.1999851`.

[10] Yoshifumi Ueno, Georg Soumagne, Akira Sumitani, Akira Endo, Takeshi Higashiguchi, and Noboru Yugami. Reduction of debris of a CO2 laser-produced Sn plasma extreme ultraviolet source using a magnetic field. *Applied Physics Letters*, 92(21):211503, 05 2008. ISSN 0003-6951. doi: 10.1063/1.2938365. URL `https://doi.org/10.1063/1.2938365`.

[11] Daniel T. Elg, John R. Sporre, Davide Curreli, Ivan A. Shchelkanov, David N. Ruzic, and Karl R. Umstadter. Magnetic debris mitigation system for extreme ultraviolet sources. *Journal of Micro/Nanolithography, MEMS, and MOEMS*, 14(1):013506, 2015. doi: 10.1117/1.JMM.14.1.013506. URL `https://doi.org/10.1117/1.JMM.14.1.013506`.

[12] S.S. Harilal, B. O'Shay, Y. Tao, and M.S. Tillack. Ion debris mitigation from tin plasma using ambient gas, magnetic field and combined effects. *Applied Physics B*, 86(3):547–553, February 2007. ISSN 1432-0649. doi: 10.1007/s00340-006-2532-3. URL `https://doi.org/10.1007/s00340-006-2532-3`.

[13] Peter Sigmund. *Particle Penetration and Radiation Effects: General Aspects and Stopping of Swift Point Charges*. Springer Nature, 01 2006. ISBN 978-3-540-31713-5. doi: 10.1007/3-540-31718-X.

[14] James F. Ziegler, Jochen P. Biersack, and Matthias D. Ziegler. *SRIM: The Stopping and Range of Ions in Matter*. SRIM, Chester, Md., 2008. ISBN 9780965420716 and 096542071X. URL `http://lib.ugent.be/catalog/rug01:001467757`.

[15] E. Aprà, E. J. Bylaska, W. A. de Jong, N. Govind, K. Kowalski, T. P. Straatsma, M. Valiev, H. J. J. van Dam, Y. Alexeev, J. Anchell, V. Anisimov, F. W. Aquino, R. Atta-Fynn, J. Autschbach, N. P. Bauman, J. C. Becca, D. E. Bernholdt, K. Bhaskaran-Nair, S. Bogatko, P. Borowski, J. Boschen, J. Brabec, A. Bruner, E. Cauët, Y. Chen, G. N. Chuev, C. J. Cramer, J. Daily, M. J. O. Deegan, T. H. Dunning, M. Dupuis, K. G. Dyall, G. I. Fann, S. A. Fischer, A. Fonari, H. Früchtl, L. Gagliardi, J. Garza, N. Gawande, S. Ghosh, K. Glaesemann, A. W. Götz, J. Hammond, V. Helms, E. D. Hermes, K. Hirao, S. Hirata, M. Jacquelin, L. Jensen, B. G. Johnson, H. Jónsson, R. A. Kendall, M. Klemm, R. Kobayashi, V. Konkov, S. Krishnamoorthy, M. Krishnan, Z. Lin, R. D. Lins, R. J. Littlefield, A. J. Logsdail, K. Lopata, W. Ma, A. V. Marenich, J. Martin del Campo, D. Mejia-Rodriguez, J. E. Moore, J. M. Mullin, T. Nakajima, D. R. Nascimento, J. A. Nichols, P. J. Nichols, J. Nieplocha, A. Otero-de-la Roza, B. Palmer, A. Panyala, T. Pirojsirikul, B. Peng, R. Peverati, J. Pittner, L. Pollack, R. M. Richard, P. Sadayappan, G. C. Schatz, W. A. Shelton, D. W. Silverstein, D. M. A. Smith, T. A. Soares, D. Song, M. Swart, H. L. Taylor, G. S. Thomas, V. Tipparaju, D. G. Truhlar, K. Tsemekhman, T. Van Voorhis, Á. Vázquez-Mayagoitia, P. Verma, O. Villa, A. Vishnu, K. D. Vogiatzis, D. Wang, J. H. Weare, M. J. Williamson, T. L. Windus, K. Woliński, A. T. Wong, Q. Wu, C. Yang, Q. Yu, M. Zacharias, Z. Zhang, Y. Zhao, and R. J. Harrison. Nwchem: Past, present, and future. *The Journal of Chemical Physics*, 152(18):184102, 2020. doi: 10.1063/5.0004997.

[16] M Stoyanov. User manual: Tasmanian sparse grids. Technical Report ORNL/TM-2015/596, Oak Ridge National Laboratory, One Bethel Valley Road, Oak Ridge, TN, 2015.

[17] Miroslav Stoyanov, Damien Lebrun-Grandie, John Burkardt, and Drayton Munster. Tasmanian, 9 2013. URL `https://github.com/ORNL/Tasmanian`.

[18] Peter J. Linstrom and William G. Mallard. The nist chemistry webbook: A chemical data resource on the internet. *Journal of Chemical & Engineering Data*, 46(5):1059–1063, 2001. ISSN 0021-9568. doi: 10.1021/je000236i. URL `https://doi.org/10.1021/je000236i`.

[19] Carsten A. Ullrich. 10 Review of ground-state density-functional theory. In *Time-Dependent Density-Functional Theory: Concepts and Applications*. Oxford University Press, 12 2011. ISBN 9780199563029. doi: 10.1093/acprof:oso/9780199563029.003.0002. URL `https://doi.org/10.1093/acprof:oso/9780199563029.003.0002`.

[20] Attila Szabo and Neil S. Ostlund. *Modern Quantum Chemistry: Introduction to Advanced Electronic Structure Theory*. Dover Publications, Inc., Mineola, first edition, 1996.

[21] Kieron Burke and Lucas O. Wagner. Dft in a nutshell. *International Journal of Quantum Chemistry*, 113(2):96–101, 2013. doi: https://doi.org/10.1002/qua.24259. URL `https://onlinelibrary.wiley.com/doi/abs/10.1002/qua.24259`.

[22] P. Hohenberg and W. Kohn. Inhomogeneous electron gas. *Phys. Rev.*, 136:B864–B871, Nov 1964. doi: 10.1103/PhysRev.136.B864. URL `https://link.aps.org/doi/10.1103/PhysRev.136.B864`.

[23] Carsten A. Ullrich. 123 The formal framework of linear-response TDDFT. In *Time-Dependent Density-Functional Theory: Concepts and Applications*. Oxford University Press, 12 2011. ISBN 9780199563029. doi: 10.1093/acprof:oso/9780199563029.003.0007. URL `https://doi.org/10.1093/acprof:oso/9780199563029.003.0007`.

[24] Carsten A. Ullrich. 45 Fundamental existence theorems. In *Time-Dependent Density-Functional Theory: Concepts and Applications*. Oxford University Press, 12 2011. ISBN 9780199563029. doi: 10.1093/acprof:oso/9780199563029.003.0003. URL `https://doi.org/10.1093/acprof:oso/9780199563029.003.0003`.

[25] Carsten A. Ullrich. 157 The frequency-dependent xc kernel. In *Time-Dependent Density-Functional Theory: Concepts and Applications*. Oxford University Press, 12 2011. ISBN 9780199563029. doi: 10.1093/acprof:oso/9780199563029.003.0008. URL `https://doi.org/10.1093/acprof:oso/9780199563029.003.0008`.

[26] W. Kohn and L. J. Sham. Self-consistent equations including exchange and correlation effects. *Phys. Rev.*, 140:A1133–A1138, Nov 1965. doi: 10.1103/PhysRev.140.A1133. URL `https://link.aps.org/doi/10.1103/PhysRev.140.A1133`.

[27] E. J. Baerends. *Perspective on "Self-consistent equations including exchange and correlation effects"*, pages 265–269. Springer Berlin Heidelberg, Berlin, Heidelberg, 2001. ISBN 978-3-662-10421-7. doi: 10.1007/978-3-662-10421-7_30. URL `https://doi.org/10.1007/978-3-662-10421-7_30`.

[28] Peter Atkins and Julio Paula. *Atkins' physical chemistry, 8th edition*. Oxford University press, 2008. ISBN 9780195685220.

[29] Roman M. Balabin. Enthalpy difference between conformations of normal alkanes: Intramolecular basis set superposition error (BSSE) in the case of n-butane and n-hexane. *The Journal of Chemical Physics*, 129(16):164101, 10 2008. ISSN 0021-9606. doi: 10.1063/1.2997349. URL https://doi.org/10.1063/1.2997349.

[30] Markus Bursch, Jan-Michael Mewes, Andreas Hansen, and Stefan Grimme. Best-practice dft protocols for basic molecular computational chemistry**. *Angewandte Chemie*, 09 2022. doi: 10.1002/ange.202205735.

[31] A. D. Becke. Density-functional exchange-energy approximation with correct asymptotic behavior. *Phys. Rev. A*, 38:3098–3100, Sep 1988. doi: 10.1103/PhysRevA.38.3098. URL https://link.aps.org/doi/10.1103/PhysRevA.38.3098.

[32] Chengteh Lee, Weitao Yang, and Robert G. Parr. Development of the colle-salvetti correlation-energy formula into a functional of the electron density. *Phys. Rev. B*, 37:785–789, Jan 1988. doi: 10.1103/PhysRevB.37.785. URL https://link.aps.org/doi/10.1103/PhysRevB.37.785.

[33] John P. Perdew, Kieron Burke, and Matthias Ernzerhof. Generalized gradient approximation made simple. *Phys. Rev. Lett.*, 77:3865–3868, Oct 1996. doi: 10.1103/PhysRevLett.77.3865. URL https://link.aps.org/doi/10.1103/PhysRevLett.77.3865.

[34] S. H. Vosko, L. Wilk, and M. Nusair. Accurate spin-dependent electron liquid correlation energies for local spin density calculations: a critical analysis. *Canadian Journal of Physics*, 58(8):1200–1211, 1980. doi: 10.1139/p80-159. URL https://doi.org/10.1139/p80-159.

[35] Takeshi Yanai, David P Tew, and Nicholas C Handy. A new hybrid exchange–correlation functional using the coulomb-attenuating method (cam-b3lyp). *Chemical Physics Letters*, 393(1):51–57, 2004. ISSN 0009-2614. doi: https://doi.org/10.1016/j.cplett.2004.06.011. URL https://www.sciencedirect.com/science/article/pii/S0009261404008620.

[36] Aron J. Cohen, Paula Mori-Sánchez, and Weitao Yang. Development of exchange-correlation functionals with minimal many-electron self-interaction error. *The Journal of Chemical Physics*, 126(19):191109, 05 2007. ISSN 0021-9606. doi: 10.1063/1.2741248. URL https://doi.org/10.1063/1.2741248.

[37] H. Levämäki, M. P. J. Punkkinen, K. Kokko, and L. Vitos. Quasi-non-uniform gradient-level exchange-correlation approximation for metals and alloys. *Phys. Rev. B*, 86:201104, Nov 2012. doi: 10.1103/PhysRevB.86.201104. URL https://link.aps.org/doi/10.1103/PhysRevB.86.201104.

[38] A. D. Becke. A multicenter numerical integration scheme for polyatomic molecules. *The Journal of Chemical Physics*, 88(4):2547–2553, 02 1988. ISSN 0021-9606. doi: 10.1063/1.454033. URL https://doi.org/10.1063/1.454033.

[39] H. Levämäki, M. Kuisma, and K. Kokko. Space partitioning of exchange-correlation functionals with the projector augmented-wave method. *The Journal of Chemical Physics*, 150 (5):054101, 02 2019. ISSN 0021-9606. doi: 10.1063/1.5078432. URL https://doi.org/10.1063/1.5078432.

[40] Keith Ball. *III.64 Optimization and Lagrange Multipliers*, pages 255–257. Princeton University Press, Princeton, 2009. ISBN 9781400830398. doi: doi:10.1515/9781400830398.255. URL https://doi.org/10.1515/9781400830398.255.

[41] Qin Wu and Troy Van Voorhis. Direct optimization method to study constrained systems within density-functional theory. *Phys. Rev. A*, 72:024502, Aug 2005. doi: 10.1103/PhysRevA.72.024502. URL `https://link.aps.org/doi/10.1103/PhysRevA.72.024502`.

[42] Michael Dolg. Effective core potential. *Modern Methods and Algoritms of Quantum Chemistry, Proceesings, Second Edition, J. Grotendorst*, 3:507–540, 01 2000.

[43] Michael Dolg. *Relativistic Effective Core Potentials*, pages 449–478. Springer Berlin Heidelberg, Berlin, Heidelberg, 2017. ISBN 978-3-642-40766-6. doi: 10.1007/978-3-642-40766-6_5. URL `https://doi.org/10.1007/978-3-642-40766-6_5`.

[44] Hyuk-Yong Kwon, Zachary Morrow, C. T. Kelley, and Elena Jakubikova. Interpolation methods for molecular potential energy surface construction. *The Journal of Physical Chemistry A*, 125(45):9725–9735, 2021. doi: 10.1021/acs.jpca.1c06812. URL `https://doi.org/10.1021/acs.jpca.1c06812`. PMID: 34730973.

[45] Miroslav K. Stoyanov and Clayton G. Webster. A dynamically adaptive sparse grid method for quasi-optimal interpolation of multidimensional analytic functions, 2015. URL `https://arxiv.org/abs/1508.01125`.

[46] Won Y. Yang, Wenwu Cao, Jaekwon Kim, Kyung W. Park, Ho-Hyun Park, Jingon Joung, Jong-Suk Ro, Han L. Lee, Cheol-Ho Hong, and Taeho Im. 3. interpolation and curve fitting, 2020. URL `https://app.knovel.com/hotlink/khtml/id:kt0137VOM3/applied-numerical-methods/interpolation-curve-fitting`.

[47] Alfio Quarteroni and Fausto Saleri. *Scientific Computing with MATLAB and Octave (Texts in Computational Science and Engineering)*. Springer-Verlag, Berlin, Heidelberg, 2006. ISBN 354032612X.

[48] Arnim Hellweg and Dmitrij Rappoport. Development of new auxiliary basis functions of the karlsruhe segmented contracted basis sets including diffuse basis functions (def2-svpd, def2-tzvppd, and def2-qvppd) for ri-mp2 and ri-cc calculations. *Phys. Chem. Chem. Phys.*, 17:1010–1017, 2015. doi: 10.1039/C4CP04286G. URL `http://dx.doi.org/10.1039/C4CP04286G`.

[49] Milton Abramowitz and Irene A. Stegun. *Handbook of Mathematical Functions with Formulas, Graphs, and Mathematical Tables.* Dover, New York, ninth dover printing, tenth gpo printing edition, 1964.

[50] A. Kramida, Yu. Ralchenko, J. Reader, and and NIST ASD Team (2023). NIST Atomic Spectra Database (ver. 5.11), [Online]. Available: `https://physics.nist.gov/asd` [Tue Jul 16 2024]. National Institute of Standards and Technology, Gaithersburg, MD., 2023. URL `https://doi.org/10.18434/T4W30F`.

[51] B.H. Bransden and M.R.C. McDowell. *Charge Exchange and the Theory of Ion-atom Collisions*. International series of monographs on physics. Clarendon Press, 1992. ISBN 9780198520207.

[52] Miroslav K. Stoyanov and Clayton G. Webster. A dynamically adaptive sparse grids method for quasi-optimal interpolation of multidimensional functions. *Computers & Mathematics with Applications*, 71(11):2449–2465, 2016. ISSN 0898-1221. doi: https://doi.org/10.1016/j.camwa.2015.12.045. URL `https://www.sciencedirect.com/science/article/pii/S0898122116000031`. Proceedings of the conference on Advances in Scientific Computing and Applied Mathematics. A special issue in honor of Max Gunzburger's 70th birthday.

[53] Jochen Garcke. Sparse grids in a nutshell. In Jochen Garcke and Michael Griebel, editors, *Sparse Grids and Applications*, pages 57–80, Berlin, Heidelberg, 2013. Springer Berlin Heidelberg. ISBN 978-3-642-31703-3.

[54] Miroslav Stoyanov. Adaptive sparse grid construction in a context of local anisotropy and multiple hierarchical parents. In *Sparse Grids and Applications-Miami 2016*, pages 175–199. Springer, 2018.

[55] Yuncai Mei and Weitao Yang. Excited-state potential energy surfaces, conical intersections, and analytical gradients from ground-state density functional theory. *The Journal of Physical Chemistry Letters*, 10(10):2538–2545, 2019. doi: 10.1021/acs.jpclett.9b00712. URL `https://doi.org/10.1021/acs.jpclett.9b00712`.

[56] Hiroki Sugisawa, Tomonori Ida, and R. V. Krems. Gaussian process model of 51-dimensional potential energy surface for protonated imidazole dimer. *The Journal of Chemical Physics*, 153(11):114101, 09 2020. ISSN 0021-9606. doi: 10.1063/5.0023492. URL `https://doi.org/10.1063/5.0023492`.

7 Appendices

7.1 Appendix A

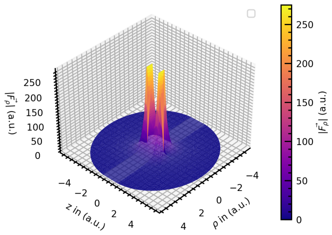

Figure 33: **F**$_\rho$*-component of Sn*$^{1+}$ *DFT potential gradient.*

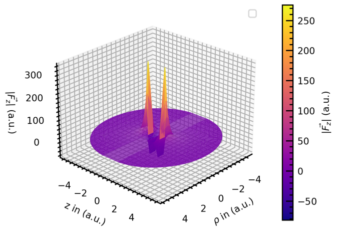

Figure 34: **F**$_z$*-component of Sn*$^{1+}$ *DFT potential gradient.*

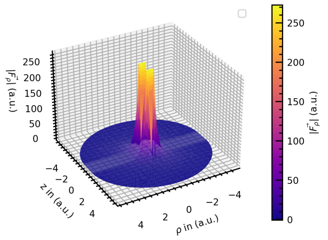

Figure 35: **F**$_\rho$*-component of Sn*$^{2+}$ *DFT potential gradient.*

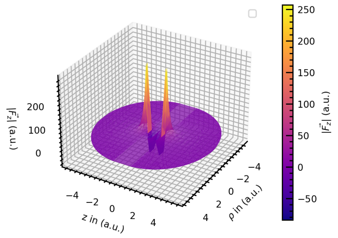

Figure 36: **F**$_z$*-component of Sn*$^{2+}$ *DFT potential gradient.*

7.2 Appendix B

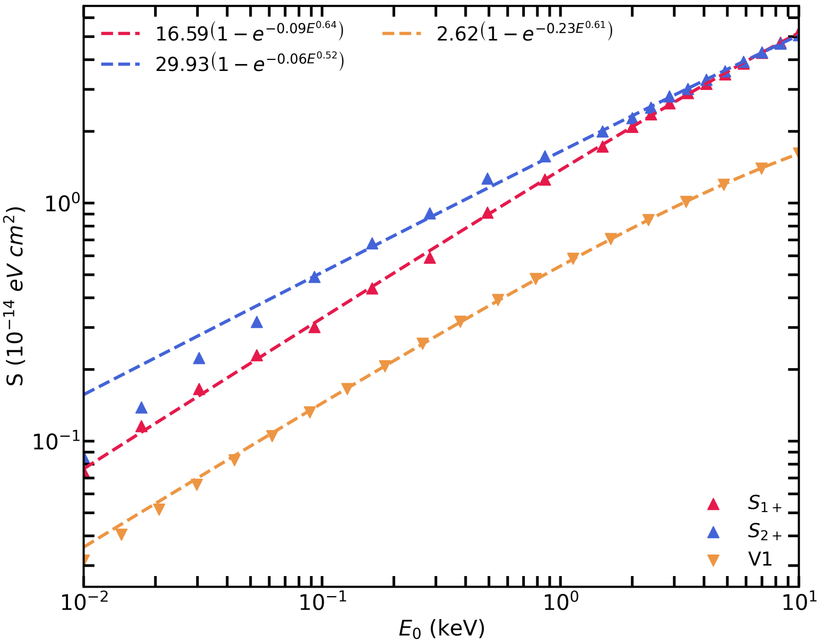

Figure 37: *Exponential stopping cross-section fits for* $Sn^{1+,2+}$ *using DFT potentials and V1*